THESIS FOR THE DEGREE OF LICENTIATE OF ENGINEERING

Towards 6 Degrees of Freedom Seakeeping Simulations Using a Fully Nonlinear Potential Flow Method

FRANCESCO COSLOVICH

Towards 6 Degrees of Freedom Seakeeping Simulations Using a Fully Nonlinear Potential
Flow Method
FRANCESCO COSLOVICH

Towards 6 Degrees of Freedom Seakeeping Simulations Using a Fully Nonlinear Potential
Flow Method
FRANCESCO COSLOVICH
Department of Mechanics and Maritime Sciences
Division of Marine Technology
Chalmers University of Technology

Abstract

In recent years, the International Maritime Organization introduced a new set of rules in order to try to reduce emissions of ships by improving their efficiency. To assess the energy efficiency of a new ship, the regulations require to estimate the Energy Efficiency Design Index (EEDI), which represent the amount of Carbon Dioxide produced per mile in relation to the amount of cargo carried, and verify that it is smaller than a prescribed value. For a proper evaluation of the EEDI, it is necessary to estimate the added resistance in waves with high accuracy. There are different ways to evaluate added resistance: empirical methods, adding a safety factor to the calm water resistance called sea margin, numerical simulations and model test experiments. Nowadays, the most used way during the design stage to do that is employing numerical simulations. Numerical simulations are not only used for the estimation of added resistance, but also to predict ship motions. If the motions are known at an early design stage, it is possible to modify the design of a ship to minimize them in order to improve the performance of the ship and to increase the safety and comfort of those who are on board.

The main objective of the PhD project is to evaluate added resistance and ship motions in oblique waves. In the work presented in this thesis, an existing fully nonlinear unsteady potential flow method is used to perform seakeeping numerical simulations in head and beam sea. Since viscosity is disregarded in potential flow methods but it is still very important for some cases, such as roll motion, viscous damping coefficients were added into the equation of motions. For the last two papers, an unstructured adaptive grid refinement, a nonlinear decomposition of the velocity potential, a formulation for the acceleration potential and a Barnes-Hut algorithm were introduced in the code. The method has been used to simulate roll motion in beam sea, parametric rolling, added resistance and ship motions in head waves as well as ship-ship interaction in calm water. Numerical results were compared with experiments and with other methods.

Overall, the method presented here proved to be able to handle the tested scenarios, showing a good agreement between the simulations and the experiments. The work summarized in this thesis contributed to a better understanding of the numerical method used and helped to outline the next steps to be taken in order to achieve numerical seakeeping simulations in 6 degrees of freedom in oblique waves.

Keywords: Fully Nonlinear Potential Flow, Seakeeping, Added Resistance, Ship Motions, Boundary Element Method

Preface

This thesis is a summary of the work carried out within the PhD project "*Added resistance and ship motions in oblique waves*" at the Division of Marine Technology, Department of Mechanics and Maritime Sciences at Chalmers University of Technology during the period October 2017 - November 2020. The project was financed by Chalmers University of Technology.

I would like to express my gratitude to my supervisors Carl-Erik Janson and Martin Kjellberg for their input, support and for always being there when I needed it. I would like to thank all the persons at Flowtech for their valuable help and inspiring conversations. I would also like to thank my colleagues at the Department for providing a nice working environment.

Thesis

This thesis consists of an extended summary and the following appended papers:

Paper A Coslovich F., Contento G., Kjellberg M. & Janson C.-E. (2018). Computations of roll motion in waves using a fully nonlinear potential flow method, In *Nav 2018. 19th international conference on ship and maritime research*

Paper B Coslovich F., Kjellberg M. & Janson C.-E. (2019). Prediction of parametric rolling for a container ship in regular and irregular waves using a fully nonlinear potential flow method, In *Marine 2019. viii international conference on computational methods in marine engineering*

Paper C Coslovich F., Östberg M. & Broberg L. (2019). Fully nonlinear potential flow method for multiple floating bodies in confined waters, In *Icsot 2019. 6th international conference on ship and offshore technology*

Paper D Coslovich F., Kjellberg M., Östberg M. & Janson C.-E. (2020). Added resistance, heave and pitch for the kvlcc2 tanker using a fully nonlinear unsteady potential flow boundary element method. *Ocean Engineering - Under Review*

CONTENTS

Part I
Extended Summary

1 Introduction

In this chapter the background and the objectives of the project will be given. An overview of other numerical methods and their evolution in time will also be presented, as well as a brief description of the method used.

1.1 Background

In order to satisfy the demands of goods across the planet, ship sizes and fleet have been increasing steadily. These growing numbers, combined with an increased awareness toward climate change and sustainable development, put new efforts on the design phase of a ship. With the aim of reducing air pollution coming from the maritime industry, in recent years the Marine Environment Protection Committee (MEPC) of the International Maritime Organization (IMO) introduced a set of rules to evaluate and improve the energy efficiency of newly built ships. The Energy Efficiency Design Index (EEDI) is the key point of these rules and it represents the amount of Carbon Dioxide CO_2 produced per mile in relation to the amount of cargo carried on board. One of the purposes of the introduction of the EEDI in the design phase was to put an end to the trend of installing oversized engines. Historically, the resistance was evaluated in calm water and then, due to the fact that the ship will sail in waves, the value was increased by $15 - 30\%$. This *sea margin* was applied to the power installed deriving from the calm water calculations, resulting in an increase of approximately 15%. The attention now, thanks to the introduction of the EEDI, is moving towards the evaluation of the resistance in an operative scenario more than in calm water. For a new design, a limiting value is calculated based on the dimensions and the type of ship and then the EEDI is evaluated for the new ship. In order to obtain a reliable value, it is necessary to predict the installed power and thus the added resistance in waves with high accuracy.

Another aspect which has been gaining more attention when designing a new ship is the possibility to predict extreme ship motions with high accuracy. If a ship experiences big amplitudes of the response in a sea state, two aspects can be in jeopardy: the performance, intended as the ability to keep the operations going or the route chosen, and the safety and comfort of the people on board. Among all motions, the most dangerous one is roll. There are a number of reason for this: first of all, the restoring moment for roll motion is considerably smaller compared to other motions. Furthermore, the damping is also small, resulting in a pronounced peak of the response when the forcing term has a frequency close to the natural one. To make things worse, the typical value of natural frequency of roll motion of ships lies in the most energetic part of a generic sea spectrum. For these reasons, even relatively small sea state can produce big amplitudes of roll motion. To study and simulate roll motion is not a simple task either: the motion is characterized by

strong nonlinearities both in the restoring and in the damping terms and it is connected to other dangerous phenomena, such as for example, parametric rolling, surf riding and broaching.

It is clear then that during the design phase it is important to be able to predict with high accuracy both the added resistance and the ship responses in a sea state. In this way, if dangerous conditions can be identified during a design, the hull shape can be optimized to reduce risks and increase safety and comfort. Furthermore, optimizing the hull to reduce added resistance will reduce fuel consumption and pollution. There are several ways to predict ship motions and added resistance during the design. The most accurate way to do so is through model tests. The main downside of this approach is that it is very expensive and time consuming and it is generally done only during an advanced stage of the design process. The simplest approach to estimate added resistance and ship motions is by mean of empirical approaches: systematic series, regression analysis and analytical methods are widely used as starting point at the beginning of a design. In between these two categories, we find numerical simulation methods. Numerical simulations have been widely used ever since computers became available. The most advanced and accurate methods used nowadays are based on Unsteady Raynolds-Averaged Navier-Stokes equations (URANS). Although they can provide very accurate results, they are not widely used during the design and in optimization processes since they require a considerable computational effort. More common methods are the ones based on the hypothesis of potential flow. Assuming that the fluid is incompressible, irrotational and inviscid allows for a considerable simplification in the equations to be solved, reducing the computational effort.

Potential flow methods have been used extensively and different levels of sophistication can be found in literature, finding different applications. They are used both to predict added resistance and ship motions, but while they work generally well for the first, care must be taken for the latter. Although roll motion is indeed characterized by a small damping, this value allows the response to be limited and then the ship not to capsize. Unfortunately, the damping is mainly generated by viscous effects, as will be discussed further in the following chapters. This means that when roll motion is simulated with a potential flow method, viscosity must be somehow introduced. Generally, this is achieved by introducing damping coefficients into the equations of motion. Furthermore, roll damping plays a fundamental role not only in the prediction of roll motion in beam sea, but also in the prediction of roll related phenomena, such as parametric rolling, broaching and surf riding. Another issue that can arise when dealing with roll motion is that nonlinearities can play an important part in the solution of the equations of motion. Historically, potential flow methods have been including some levels of linearization and only in recent years fully nonlinear potential flow methods started to be developed and used.

In this thesis, investigations of the performance of two existing codes, SHIPFLOW Motions 6 and SHIPFLOW Motions 7, are presented. In the papers appended here, the two codes have been used to evaluate roll motion, parametric rolling, ship-ship interaction in calm water and added resistance for a ship sailing in a seaway. The project is the continuation of another Ph.D. project, presented in Kjellberg, 2013. Several aspects have been modified from a numerical point of view but the mathematical modeling and the

structure of the program are the same.

1.2 Literature Review

Several methods and techniques have been developed to predict added resistance with potential flow methods. Among the most used ones, we can find far-field and near-field approaches. The far-field method is based on considerations on energy flux through a control surface and was initially introduced by Maruo, 1957 and modified in the following years by himself and by Joosen, 1966. Gerritsma and Beukelman, 1972 introduced the radiated energy approach to evaluate added resistance in head waves, following more or less the method proposed by Maruo. Some years later, Salvesen, 1974 combined this method with a strip theory method, which was capable of obtaining better results in terms of prediction of ship motions, achieving better results for added resistance too. In this way, it was possible to understand the importance of properly predict ship motions to have a reliable value for added resistance.

Near-field methods obtain added resistance through a direct integration of the hydrodynamic pressure on the hull. This approach has been finding more success in the last couple of decades, with the attention shifting towards time-domain potential flow methods. The first near-field method was proposed by Faltinsen et al., 1980. Due to some limitations of the method in the short waves range, an analytical correction was proposed for those wave lengths. In more recent years, Joncquez et al., 2008 and Liu et al., 2011 computed added resistance for several hulls using a number of 3D panel methods, applying both the far-field and near-field approaches to compare results. Joncquez used a 3D time domain high order boundary element method with Neumann-Kelvin (NK) and Double Body (DB) linearizations to compute the forces while Liu used a 3D frequency domain panel method and a hybrid time domain Rankine source-Green function method. Also Kim et al., 2012 computed added resistance using both approaches for several hull forms, where a time domain Rankine panel method with NK and DB linearizations was used. The comparison with experimental data showed that the near-field method gives better results for long waves, while the far-field method is better suited for short waves. Guha and Falzarano, 2015 used a three dimensional frequency domain Green function panel method to evaluate the added resistance with a near-field approach for several hulls. The results were compared with other numerical methods and with experimental results.

When simulating roll motion with a potential flow method, viscosity has to be introduced to take into account roll damping, which is largely influenced by viscous effects. The most common way to account for roll damping is to introduce damping coefficients into the equation of roll motion. These models are polynomial expressions where the damping coefficients are combined with roll angle velocity. More complex and accurate formulations include also the angle dependency. An investigation on different models and their influence on the solution can be found in Bass and Haddara, 1988. While damping coefficients are generally assumed to be constant for a range of incoming wave frequencies and wave steepness, Contento et al., 1996 proved that introducing a dependency on these quantities allows to achieve better results. As far as the evaluation of the damping coefficients is concerned, several methods are available in literature. A summary of some

of the most used techniques up to today was presented in Himeno, 1981. The report focuses on models which predict damping coefficients based on ship characteristics more than operative conditions. Falzarano et al., 2015 as well summarized the most used models to estimate damping coefficients and investigated which models are used by the most common commercial seakeeping codes. There are also methods which evaluate damping coefficients analysing model test results. ITTC, 2011 uses a polynomial representation of peaks envelop of roll decay tests. Although this method is straightforward to implement, it presents some limitations: to have an accurate evaluation a high number of peaks is needed. This introduces errors due to measurements, since the roll angle gets smaller and uncertainties get bigger, and due to reflection of waves from the boundaries which effect the roll angle. Bass and Haddara, 1988 use a least square methods to find the best set of damping and restoring coefficients which fit the experimental data. This technique uses a time series of roll decay. Francescutto and Contento, 1999 use use a similar procedure, which was extended to take into account RAOs for roll motion in beam sea.

Historically, the vast majority of potential flow methods introduced some linearizations in the equations to be solved. This was done to further simplify the problem, since the computational power was quite limited. For a number of applications though, linearizing the problem did not introduced significant errors and the results obtained could be considered reliable, especially if we keep in mind that the tools were the state of the art. Furthermore, the margin for optimizing a design were quite significant. Thanks to a growing computational power, in recent years a number of fully nonlinear potential flow methods have started to be developed. In these methods, double model and free surface linearizations are generally disregarded: the boundary conditions include also nonlinear terms and the positions of the hull and of the free surface are updated at each time step. Engsig-Karup et al., 2009 developed a fully nonlinear 3D potential flow method to simulate water waves and Ducrozet et al., 2010 extended it for wave-wave and wave-structure interaction in the case of a fixed circular cylinder. Mola et al., 2017 developed a fully nonlinear potential flow method adding a pressure patch in the stern area and used it to evaluate the performances of different hulls in calm water.

1.3   Objectives

In the project summarized in this report, an unsteady fully nonlinear potential flow method has been used to predict added resistance and ship motions for several hulls in different conditions. The main objective of this project is to predict ship motions and added resistance in oblique waves with high accuracy. To achieve that, we started from simpler cases and different conditions had been analyzed separately. Roll decay was simulated for a container ship and for a *Series* 60 hull, which was used to simulate roll motion in beam sea as well. Parametric rolling was simulated for a container ship in head and following waves for monochromatic and three components regular waves as well as irregular waves. A ship-ship interaction study was carried out for two tankers replicating a lightering operation. Finally, added resistance and ship motions were studied for the KVLCC2 tanker in head waves.

The code used is a fully nonlinear potential flow method: the free surface boundary

conditions are fully nonlinear, the position of the hull and of the free surface are updated at each time step and the forces are evaluated on the instantaneous wetted surface. The method aims at filling the gap between partially nonlinear potential flow codes, where simplifications are made to keep the computational effort low at the expenses of the accuracy of the results, and viscous solvers, where high accuracy is reached but the time needed to run a simulation can be significant.

The main vision of Chalmers is "Chalmers for a sustainable future". With this vision, Chalmers seeks to meet the needs for a ecological, social and economic sustainability. As mentioned in Section 1.1, if extreme motions are experienced by the ship, the comfort and safety of the people on board can be at risk. It is clear then that being able to identify these possible situations and take action against them during a design phase, will improve the working conditions of those who work on board. With reference to the Sustainable Development Goals (SDGs), this project is linked to the SDG 8, *decent work and economic growth*[1]. Furthermore, the code can be used to estimate added resistance with high accuracy and can be used in an optimization process to modify the hull to increase its efficiency, reduce fuel consumption and thus emissions. With this perspective, the project can be linked to the SDG 13, *climate action*[2].

1.4   The Method

The code is based on the work presented in Kjellberg et al., 2011, Kjellberg et al., 2012 and Kjellberg, 2013 and it has been extended during the project. The starting point is a fully nonlinear unsteady potential flow method which uses a Mixed Eulerian-Lagrangian (MEL) approach for the evolution in time. As it will be described more in the following chapters, major changes have been implemented in the code between the first and last two papers.

In the first two papers the method used a structured mesh resolution to discretize the domain. Once the dimensions of the quadrilateral panels of the free surface and of the hull were chosen, the number of panels remained fixed throughout the simulation. The main advantage of this approach is that it is easy to implement. The main limitation, on the other hand, is that if a fine mesh resolution is required on the free surface, an unnecessarily high number of panels will be used. In fact, there are portions of the domain where this resolution is not needed: far upstream and sideways the influence of the hull is generally quite limited. For this reason, in the last two papers an unstructured mesh was used. This mesh was combined with an adaptive grid refinement algorithm, where the panels are divided into smaller ones in areas of interest and where a higher resolution is needed to properly solve the hydrodynamics. Figure 1.1 shows a structured and an unstructured mesh.

Another major change in the code is the decomposition of the velocity potential. In the last two papers, the velocity potential is obtained as the sum of the potential of the incoming waves and the potential due to the disturbance of the ship. Since the potential

---

[1] Promote sustained, inclusive and sustainable economic growth, full and productive employment and decent work for all.

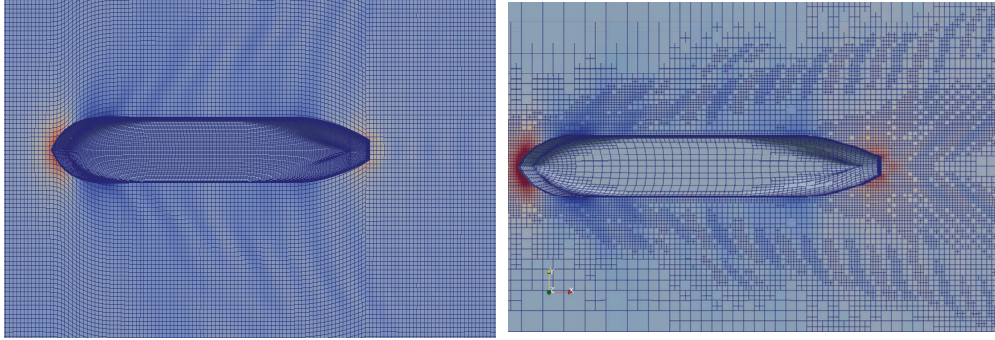[2] Take urgent action to combat climate change and its impacts

Figure 1.1: *Comparison between structured and unstructured adaptive mesh.*

of the incoming waves is known *a priori*, then it is enough to solve for the potential of the disturbance. In this way, a considerable gain is obtained in terms of computational effort.

Another implementation which improved the code in terms of computational effort is the introduction of a Barnes-Hut algorithm. With this algorithm, panels are grouped together into nodes and when solving the system, all the panels belonging to one node are treated as a single panel if they are far enough from a point of interest. In this way, the computational effort of the simulations is reduced from an order of $O(n^2)$ to $O(n \log(n))$. The more panels are include in one node, the higher the gain in terms of computational effort, at the expenses of the accuracy.

Last but not least, the final major modification to the code is related to how the hydrodynamic pressure is evaluated. In the panel method, the pressure is obtained using the unsteady Bernoulli equation. This equation presents a term which is the derivative in time of the velocity potential. In the first two papers, this term is evaluated using a backward difference scheme. This way of evaluating the pressure can result in unstable solutions and crashes of the code, especially for flat sterns ships. To improve this aspect, a formulation for the acceleration potential was introduced. With this method, a new boundary element method for the time derivative of the velocity potential is introduced and solved.

1.5   Summary of the Papers

In paper A roll decay for a post-panamax container ship and roll motion in beam sea for a *Series* 60 hull were studied. In order to take into account viscous effects which are not included into a potential flow method, two techniques to evaluate damping coefficients were used. Damping coefficients are then included into the equations of motion. One technique estimates these coefficients starting from the main dimension and inertial characteristics of the ship, while the other obtains them through analysing experimental data available. A general good agreement between simulations and experiments was found for both cases.

In paper B, the SAFEDOR benchmark study presented in Papanikolaou and Spanos,

2009 on parametric rolling was replicated. Both head and following waves were simulated for a container ship and the numerical results were compared with experimental results and with other codes which were used in the benchmark study. Damping coefficients were included in the equations of motion using the same methods of the paper A.

For paper C, the new version of the code was used. In this paper an analysis of ship-ship interaction in shallow water was performed. A benchmark study on lightering operations was replicated and the numerical simulations were compared with experimental results available and with results from viscous computations. Some discrepancies due to an incorrect prediction of the forces were noted in the computations.

A thorough investigation of the grid resolution was carried out for a KVLCC2 hull sailing in head waves at the design speed and is presented in paper D. The influence of time step size was also investigated. Very good agreement with experimental results carried out at SSPA Sweden AB was found, both in terms of ship motions and of added resistance.

2 Mathematical Model

In this chapter the mathematical model of the code is presented. The mathematical model presented here is adopted for all papers, except for Sections 2.5 and 2.6, which are implemented for papers C and D only.

2.1 Coordinate Systems

To describe the position and the orientation of the hull and the forces acting on it, three coordinate systems are used. When describing a general free surface problem, an earth fixed coordinate system is used. With the introduction of a floating body, two more systems are introduced in order to facilitate the evaluation of forces and motions of the body. One of these system is an inertial system associated with the position of the body and the other one is a body-fixed reference system. The systems used are:

- (O, x, y, z): an earth-fixed right-handed coordinate system, with its origin at an arbitrary point on the initial free surface with the z-axis pointing upward, perpendicular to the horizontal plane representing the calm water condition. The free surface evolution and the equations governing the flow are expressed in this system.

- (O_B, x_B, y_B, z_B): a body fixed coordinate system, with its origin at the center of gravity of the ship, with the x-axis pointing toward the bow and the z-axis pointing upward. This system is used to express the forces acting on the ship.

- (O_I, x_I, y_I, z_I): a body-fixed inertial coordinate system. This system is centered on the vertical line passing through the center of gravity and placed on the waterplane. It is only allowed to move on the horizontal plane and it is used to describe the position of the body with respect to (O, x, y, z).

2.2 Boundary Value Problem

In order to simulate the flow around a hull sailing in a seaway, the Navier-Stokes equation has to be solved. Since a direct solution of the Navier-Stokes equations is not possible, simplifications must be introduced. If we assume that the fluid is homogeneous, inviscid, incompressible and irrotational, there exists a scalar quantity referred to as velocity potential ϕ, that describes the flow. The velocity potential is defined as:

$$\nabla \phi = (\frac{\partial \phi}{\partial x}, \frac{\partial \phi}{\partial y}, \frac{\partial \phi}{\partial z}) = (u, v, w) = \boldsymbol{u} \tag{2.1}$$

Substituting equation (2.1) into the continuity equation for incompressible fluids, we obtain Laplace's equation:

$$\nabla^2 \phi = 0 \tag{2.2}$$

This differential equation is considerably simpler than the Navier-Stokes equation, since it is a linear partial derivative equation. It is possible to know the flow on the domain by

solving Equation 2.2. In order to solve it, we are going to introduce boundary conditions on the domain and in this way we define a Boundary Value Problem (BVP).

2.2.1 Free Surface Boundary Conditions

On the free surface, the Kinematic Boundary Condition (KBC) and Dynamic Boundary Condition (DBC) are applied. Part of the nonlinearities present in the method are introduced in the KBC and DBC.

Kinematic Boundary Condition

The kinematic boundary condition grants that there is no flow through the free surface, meaning that a particle belonging to the free surface will always belong to it. Being $\boldsymbol{x} = (x, y, z)$ the position of a fluid particle on the free surface in the (O, x, y, z) Cartesian coordinate system, the fully nonlinear kinematic boundary conditions is:

$$\frac{D\boldsymbol{x}}{Dt} = (\frac{dx}{dt}, \frac{dy}{dt}, \frac{dz}{dt}) = (u, v, z) = \nabla\phi \tag{2.3}$$

$\frac{D}{Dt}$ is the material derivative and is defined as:

$$\frac{D}{Dt} = \frac{\partial}{\partial t} + \nabla\phi \cdot \nabla \tag{2.4}$$

Dynamic Boundary Condition

The dynamic boundary condition does not allow for a jump on the pressure on the free surface. This means that the hydrodynamic pressure on the free surface is equal to the atmospheric pressure. It derives from the unsteady Bernoulli equation and is defined as:

$$\frac{D\phi}{Dt} = -gz + \frac{1}{2}\nabla\phi \cdot \nabla\phi - \frac{p_a}{\rho} \tag{2.5}$$

where g is the gravitational acceleration, ρ is the fluid density, p_a is the atmospheric pressure and $\frac{D}{Dt}$ is the material derivative as defined in 2.4.

2.2.2 Body Boundary Conditions

Boundary conditions have to be applied on all the boundaries of the domain. Therefore they will be imposed on the bottom and on the floating object too. Neumann-type boundary conditions are applied on the instantaneous wetted body surface and on the bottom of the domain, imposing no flow through such surfaces, *i.e.* impermeability condition:

$$\nabla\phi \cdot n = \frac{\partial\phi}{\partial n} = n \cdot (\boldsymbol{u} + \boldsymbol{\omega} \times \boldsymbol{r}) \tag{2.6}$$

where n is the normal to the surface pointing into the fluid domain, $\boldsymbol{u}$ and $\boldsymbol{\omega}$ are the translational and angular velocities and $\boldsymbol{r}$ is the distance between the surface and the center of rotation.

Following the same criteria, on the bottom an impermeability condition is applied as well:

$$\nabla\phi \cdot n = 0 \tag{2.7}$$

2.3 Unsteady Pressure and Forces

When solving the BVP defined in Section 2.2, the velocity potential and the velocities will be known on the fluid domain and on the floating body, as it will be described in Chapter 3. Once these quantities are known, the forces acting on the hull will be evaluated integrating the pressure on the instantaneous wetted surface.

The total pressure on the hull is given by Bernoulli's unsteady equation:

$$p = -\rho(\frac{\partial\phi}{\partial t} + \frac{1}{2}\left|\nabla\phi\right|^2 + gz) \tag{2.8}$$

The time derivative of the velocity potential, which represents the unsteady term, can be evaluated in several ways. In this project two methodologies have been followed. For papers A and B, this quantity has been obtained using a finite difference second order backward scheme. The advantage of using this technique is that it is straightforward to implement. There are two major downsides: first of all, by doing so, the motion of the body and the one of the fluid are decoupled. The second one is that instabilities in the solution are introduced. To solve this problem, another approach has been followed for papers C and D: a new BVP is introduced and by solving it the acceleration potential is found. This method will be further explained in Section 2.5.

Once the pressure is known, the hydrodynamic forces acting on the body can then be computed by integrating the pressure over the wetted hull surface:

$$\boldsymbol{F} = -\iint\limits_{S_b} p\vec{n}\,dS, \tag{2.9}$$

where $\boldsymbol{F} = (F_1, F_2, F_3)$ and the moments according to

$$\boldsymbol{F} = -\iint\limits_{S_b} p\left(\boldsymbol{r}\times\boldsymbol{n}\right)\,dS, \tag{2.10}$$

where $\boldsymbol{F} = (F_4, F_5, F_6)$.

When a ship is sailing in a seaway, a number of forces acting on it arise: radiation and diffraction forces, effects from forward speed and incident forces from the wave system. This decomposition of the force into components is typically used in linear and partial nonlinear methods. Although it is a simpler approach, it misses information, such as nonlinear interaction effects. In a nonlinear approach all effects are accounted for integrating the unsteady pressure over the hull to obtain the forces instead.

2.4 Rigid Body Motions

Once the forces are evaluated for the floating body, it is possible to obtain the motions. Ship motions are evaluated in the body fixed coordinate system (O_B, x_B, y_B, z_B), where the forces are evaluated.

Velocities in the body fixed coordinate system are here defined by the vectors $\boldsymbol{u} = (u, v, w)$ and $\boldsymbol{\omega} = (p, q, r)$, where $\boldsymbol{u}$ represent translational velocities and $\boldsymbol{\omega}$ represent angular velocities. In the inertial coordiante system, velocities are defined by the vectors $\boldsymbol{U} = (\dot{x}, \dot{y}, \dot{z})$ and $\boldsymbol{\Omega} = (\dot{\varphi}, \dot{\theta}, \dot{\psi})$, where $\boldsymbol{U}$ represent translational velocities and $\boldsymbol{\Omega}$ represent angular velocities.

The transformation from the body fixed coordinate system into the inertial coordinate system is achieved through the transformation matrices:

$$\boldsymbol{L} = \begin{bmatrix} c\theta c\psi & s\varphi s\theta c\psi - c\varphi s\psi & c\varphi s\theta c\psi + s\varphi s\psi \\ c\theta s\psi & s\varphi s\theta s\psi + c\varphi c\psi & c\varphi s\theta s\psi - s\varphi c\psi \\ -s\theta & s\varphi c\theta & c\varphi c\theta \end{bmatrix} \tag{2.11}$$

$$\boldsymbol{B} = \begin{bmatrix} 1 & s\varphi t\theta & c\varphi t\theta \\ 0 & c\varphi & -s\varphi \\ 0 & s\varphi/c\theta & c\varphi/c\theta \end{bmatrix} \tag{2.12}$$

where c, s and t stand for cosine, sine and tangent respectively, so that

$$\boldsymbol{U} = [\boldsymbol{L}]\boldsymbol{u} \tag{2.13}$$

$$\boldsymbol{\Omega} = [\boldsymbol{B}]\boldsymbol{\omega} \tag{2.14}$$

Their inverse forms are used for transformation from the inertial coordinate system into the body fixed coordinate system:

$$\boldsymbol{u} = [\boldsymbol{L}]^{-1}\boldsymbol{U} \tag{2.15}$$

$$\boldsymbol{\omega} = [\boldsymbol{B}]^{-1}\boldsymbol{\Omega} \tag{2.16}$$

The equation of motion represent the equilibrium between the inertial, gravitational and hydrodynamic forces. With m being the mass of the body and I_{ij} being the mass moments of inertia, $\boldsymbol{F} = (F_1, F_2, F_3, F_4, F_5, F_6)$ being hydrodynamic forces and moments and $\boldsymbol{F}_g = (F_{g1}, F_{g2}, F_{g3})$ being gravitational forces, the equation of motion for a rigid body can be expressed as:

$$\begin{aligned} F_1 + F_{g1} &= m(\dot{u} + qw - rw) \\ F_2 + F_{g2} &= m(\dot{v} + ru - pw) \\ F_3 + F_{g3} &= m(\dot{w} + pv - qu) \\ F_4 &= I_{xx}\dot{p} + I_{xy}\dot{q} + I_{xz}\dot{r} + (I_{zz} - I_{yy})qr - I_{xy}rp + I_{zx}pq + I_{yz}(q^2 - r^2) \\ F_5 &= I_{yx}\dot{p} + I_{yy}\dot{q} + I_{yz}\dot{r} + (I_{xx} - I_{zz})rp - I_{yz}pq + I_{xy}qr + I_{zx}(r^2 - p^2) \\ F_6 &= I_{zx}\dot{p} + I_{zy}\dot{q} + I_{zz}\dot{r} + (I_{yy} - I_{xx})pq - I_{zx}rq + I_{yz}rp + I_{xy}(p^2 - q^2) \end{aligned} \tag{2.17}$$

11

2.4.1 Roll Motion

Roll motion plays a fundamental role when assessing the seakeeping capabilities of a ship, since it can easily lead to extreme motions and dangerous situations. Roll motion is characterized by small restoring moment and by an even smaller damping ability. The consequence of this is that even in moderate sea states there can be big roll motion amplitudes, especially when the frequency of the incoming waves is close to the roll natural frequency of the hull. In literature different ways of modelling roll motion can be found, based on the level of approximation introduced. For sake of simplicity, let us focus here on the 1 Degree Of Freedom (DOF) equation of motion, meaning that we will disregard the coupling terms. In the following we will refer to the roll angle as φ. Considering the 1 DOF equation for roll, we have:

$$I_{xx}\ddot{\varphi} = -\iint_{S_b} p(\mathbf{r} \times \mathbf{n}) \cdot \mathbf{i} \, dS \tag{2.18}$$

where $\ddot{\varphi}$ is the roll acceleration and $\boldsymbol{i}$ is the vector representing the x-axis in the body-fixed coordinate system $\boldsymbol{i} = (1, 0, 0)$.

Equation 2.18 can be simplified if we apply the superposition principle. Although we might include nonlinear functions for some terms, we are still supposing that all the components are independent from one another, linearizing in fact the system. Splitting Equation 2.18 into single components results in:

$$I_{xx}\ddot{\varphi} = -M_{add}\ddot{\varphi} - B(\dot{\varphi}) - C(\varphi) + M(t) \tag{2.19}$$

where M_{add} is the added mass, $B(\dot{\varphi})$ is a function for the damping, $C(\varphi)$ is a function the restoring term and $M(t)$ is the forcing term. The damping and restoring terms can be further simplified, assuming a linear function for them. This would be the most simplified formulation for the roll motion. The main problem with it, related to the highly nonlinear behaviour of restoring and damping, is that it assumes the amplitudes of the motion to be small, introducing a considerable error.

With the method used in this project, forces are evaluated on the instantaneous wetted surface. This means that all terms except the damping are implicitly evaluated in Equation 2.18. The damping term is not accounted for since it is mainly due to viscous effects and we are working under the hypothesis of potential flow, hence supposing the fluid to be inviscid. The energy dissipation indeed is mostly affected by friction and vortices creation, while the wave making component is limited: the extreme case of a cylinder rolling in calm water will not produce any waves. Numerical simulations of roll motion using potential flow methods have to account for viscous damping. The most common way to do it, is to introduce damping coefficients in the equation of roll motion. Supposing a general nonlinear function for the damping term, Equation 2.18 becomes:

$$I_{xx}\ddot{\varphi} = -\iint_{S_b} p(\mathbf{r} \times \mathbf{n}) \cdot \mathbf{i} \, dS - B(\dot{\varphi}) \tag{2.20}$$

2.5   Acceleration potential

The evaluation of the time derivative of the velocity potential can lead to instability and formally decouples the motion of the body from the one of the fluid. One way of getting around this is to directly calculate $\frac{\partial \phi}{\partial t}$ from its boundary conditions. In the work presented here the method presented by Kang and Gong, 1990 has been used for papers C and D, after major changes had been included in the code.

This method is based on a modal decomposition of the rigid body acceleration components, which implies the solution of $n+1$ additional BVP where n is the number of degrees of freedom of the rigid body. This means that a new BVP has to be solved for each degree of freedom, where the unknown is the acceleration potential. A downside of this method is that the computational effort will increase. Another inconvenient is that the free surface boundary conditions have to be expressed in the body-fixed coordinate system, introducing some numerical error, as reported in Bandick and Beck, 2010.

2.6   Nonlinear decomposition

To increase the efficiency of the computations, a nonlinear decomposition of the solution, as described by Ducrozet et al., 2010, has been introduced in the method. This approach has been used in papers C and D. The free surface elevation ζ and the velocity potential ϕ are decomposed into an *incident* and a *scattered* part, where the incident terms describe the undisturbed incident wave field and the scattered terms describe any disturbance to the incident wave field:

$$\begin{aligned} \zeta &= \zeta^I + \zeta^S \\ \phi &= \phi^I + \phi^S, \qquad \vec{x} \in D \end{aligned} \tag{2.21}$$

In practice this means that for a computation with no incident wave field, i.e. calm water, the incident wave elevation (ζ^I) and the incident velocity potential (ϕ^I) are zero and the total solution is represented fully by the scattered part. In the presence of an incident wave field, ζ^S and ϕ^S contain the disturbance by the hull and the effects of the interactions between this disturbance and the incident wave field.

The decomposition results in a new formulation of the free surface boundary conditions:

$$\frac{D\boldsymbol{x}}{Dt} = \nabla \left(\phi^I + \phi^S \right) \tag{2.22}$$

$$\frac{D\phi}{Dt} = -gz + \frac{1}{2} \nabla \left(\phi^I + \phi^S \right) \cdot \nabla \left(\phi^I + \phi^S \right) - \frac{p_a}{\rho} \tag{2.23}$$

Since the incident wave field is a solution to the Laplace problem, the Laplace problem for the scattered solution becomes:

$$\begin{aligned} \nabla^2 \phi^S &= 0, & \boldsymbol{x} &\in D \\ \phi^S &= \phi^S, & \boldsymbol{x} &\in S_f \\ \nabla(\phi^I + \phi^S) \cdot \boldsymbol{n} &= \boldsymbol{n} \cdot (\boldsymbol{v} + \boldsymbol{\omega} \times \boldsymbol{r}), & \boldsymbol{x} &\in S_b \end{aligned} \tag{2.24}$$

Note that the free surface boundary conditions (2.22) and (2.23) have to be evaluated at the total surface elevation $\zeta = \zeta^I + \zeta^S$. This means that the incident part of the potential ϕ^I has to be evaluated at a position other than the surface elevation of the undisturbed incident wave ζ^I. Also note that the free surface evolution tracking in time is done for the total solution (scattered plus incident) in order not to loose nonlinear effects.

The pressure can finally be calculated in two different ways, where the scattered part is either evaluated by means of backward-differences $\frac{\partial \phi_D^S}{\partial t}$ or based on the acceleration potential $\frac{\partial \phi_P^S}{\partial t}$:

$$p_D = -\rho \left(\frac{\partial \phi^I}{\partial t} + \frac{\partial \phi_D^S}{\partial t} + \frac{1}{2} |\nabla \phi|^2 + gz \right). \tag{2.25}$$

$$p_P = -\rho \left(\frac{\partial \phi^I}{\partial t} + \frac{\partial \phi_P^S}{\partial t} + \frac{1}{2} |\nabla \phi|^2 + gz \right). \tag{2.26}$$

3 Numerical Method

In this chapter the description of how the mathematical model has been implemented in the code is presented. As mentioned already, there are some major changes between the first two papers and the last two, especially when it comes to the mesh of the free surface. In this chapter the numerical scheme will be presented and the differences between the two versions of the code will be highlighted.

3.1 Boundary Element Method

The BVP described in Section 2.2 is solved using a *Boundary Element Method* (BEM). This code used for this work is a boundary element method and is based on Hess and Smith, 1967. The domain is discretized by means of flat quadrilateral panels with an unknown constant strength source distribution. To obtain the source strength σ, the Green's function is used. Given two points P and Q on the domain, the Green's function is defined as:

$$G = \frac{1}{4\pi r(P,Q)} \tag{3.1}$$

where

$$r(P,Q) = \sqrt{(x_P - x_Q)^2 + (y_P - y_Q)^2 + (z_P - z_Q)^2} \tag{3.2}$$

If there are only sources on the boundary of the domain, the velocity potential at a point P becomes, using Green's theorem:

$$\phi(P) = -\frac{1}{\alpha} \iint_S \left[G \frac{\partial \phi(Q)}{\partial n} \right] dS \tag{3.3}$$

where S is the boundary of the domain, n is the normal direction of the panel, α is the solid angle and G is the Green's function and represents the potential of a source of unitary strength. The solid angle α is equal to 1 if P is inside the domain and $\frac{1}{2}$ if P belongs to the boundary. Substituting the Green's function into Equation 3.3, we get then the velocity potential for a point P in the fluid domain:

$$\phi(P) = -\frac{1}{\alpha} \iint_S \left[\frac{1}{r(P,Q)} \sigma(Q) \right] dS \tag{3.4}$$

To solve the velocity potential on the domain, we need to know the strength of the sources placed on the computational domain. Looking at the boundary conditions defined in Chapter 2, we can identify two conditions: one where the velocity potential is know, which is the free surface, and one where the normal derivative of the potential is given at each time step, corresponding to the body. We can then define two equations that will be used to solve the BVP:

$$-\frac{1}{\alpha} \iint_S \frac{1}{r(P,Q)} \sigma(Q) \, dS = \phi_{\mathrm{bc}}(P) \quad \text{for } P \in S_{\mathrm{D}} \tag{3.5}$$

and

$$-\frac{1}{\alpha} \iint\limits_{S} \frac{\partial}{\partial n} \left(\frac{1}{r(P,Q)} \right) \sigma(Q) \, dS = \frac{\partial \phi_{\mathrm{bc}}(P)}{\partial n} \quad \text{for } P \in S_{\mathrm{N}} \qquad (3.6)$$

where

σ	an unknown source strength,
ϕ_{bc}	the given velocity potential at P,
$\frac{\partial \phi_{\mathrm{bc}}}{\partial n}$	the given normal velocity at P,
S_{D}	a surface on which ϕ_{bc} is given,
S_{N}	a surface on which $\frac{\partial \phi_{\mathrm{bc}}}{\partial n}$ is given.

In this way a linear system can be set up and by solving it, the source strength will be known. Once the source are known, it is possible to obtain the potential on those panels where the normal derivative was known and vice versa.

3.2 Free Surface Evolution

In the current method, the time dependency is introduced by the fully nonlinear boundary conditions on the free surface. The evolution in time of the free surface is obtain with a *mixed Eulerian-Lagrangian* (MEL) approach, introduced by Longuet-Higgins and Cokelet, 1976. Markers are associated at each panel and they are used to track the evolution in time of the free surface and the velocity potential. With this methodology, each step is divided into two sub-steps:

1. Eulerian step: the BVP is solved by means of the BEM. At the end of this step the velocity potential and velocity at the markers are calculated.

2. Lagrangian step: the free surface boundary conditions defined in Equations 2.3 and 2.5 are integrated in time and the position of the markers is updated.

Once the Lagrangian step is finished, a new free surface mesh is generated. Depending on whether a structured or unstructured mesh is used, a different procedure will be adopted. Both methods though interpolate the position of the markers to obtain the surface elevation. By enforcing a single-valued free surface, thin-plate splines can be used for this purpose. In addition, the boundary conditions for the next Eularian step are evaluated by interpolating the velocity potential of the markers. To obtain the evolution in time of the free surface, an integration scheme is introduced. A fourth order Runge-Kutta is used for the first four time steps of the simulation, while a fourth order Adams-Bashforth-Moulton method is used for the rest.

3.3 Free Surface Mesh Generation

The code presented here uses an automatic free surface mesh generation. The mesh generator, which is embedded in the code, re-evaluates the free surface at the end of each Lagrangian step while the body is meshed before the first time step only. This is necessary since the code is fully nonlinear and thus forces and velocities have to be evaluated on
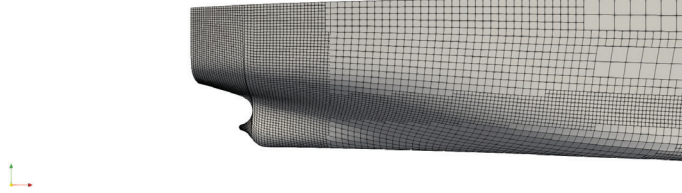
Figure 3.1: *Mesh resolution for KVLCC2.*

the instantaneous positions. The domain is discretized with quadrilateral panels and two different approaches can be used: structured and unstructured mesh generation.

3.3.1 Structured Mesh Generation

In papers A and B a structured mesh is used to discretize the fluid domain. This approach is based on the work of Janson, 1997. The panels can be stretched in the longitudinal and transverse directions but their shape remains the same during the course of a simulation. Each panel has an associated marker which is used to trace the changes of the panel and to define its position during the interpolation for advancing in time. The positions of the markers are used to create the free surface by mean of splines in tension passing through the markers: when the integration in time is performed and the boundary conditions are updated for the free surface on the position of the markers, the mesh has to be updated accordingly. In order to do that, the position of several markers is used to obtain the new shape of the free surface.

3.3.2 Unstructured Mesh Generation

To increase efficiency and accuracy of the computations, an adaptive mesh refinement has been introduced and it is used for papers C and D. The adaptive mesh refinement is applied on the free surface, while on the hull the panelization is kept constant during a simulation. An initial refinement is applied on the hull too, in areas where a higher resolution might be needed, based on local curvature. Furthermore, a refined band on panels is added around the waterline and on the bow and stern, to facilitate solving the flow in critical areas. An example of the refinement around the stern for a KVLCC2 can be seen in Figure 3.1.

On the free surface, an adaptive refinement scheme is used at each time step if a criterion is met. Every time a criterion is met for a panel, this is split recursively into four sub-panels. The user specifies a maximum level of refinement which represents the maximum number of subdivisions a panel can go through. There are two criteria that trigger the refinement: one is connected with the intersection between the free surface and the hull and the second one is is based on the curvature of the free surface. Regardless of
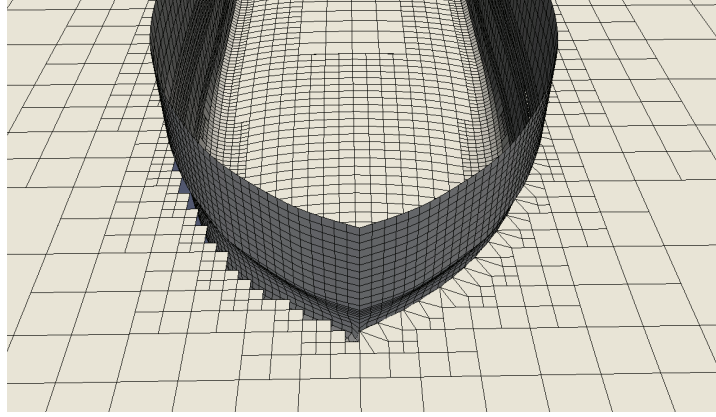
Figure 3.2: *Detail of the intersection between free surface and the hull.*

the criterion though, there will never be two neighboring panels with more than one level difference between the two in order to guarantee a smooth mesh.

On the intersection between the free surface and the hull, the panels have the maximum level of refinement. Moving away from the hull, the levels are linearly decreased by one unit. The influence of the hull on the mesh can easily be seen on an initial time step for a calm water case, Figure 3.3a. Special care must be taken for the panels on the intersection between the hull and the free surface: when a panel is split into its four sub-panels due the presence of the hull, one of these can end up being completely inside the hull. This sub-panel will then be discarded and the refinement will continue on those cut by the intersection between free surface and the hull. Since the domain is discretized by quadrilateral panels, at the end of this process there will still be gaps between the free surface and the hull, even for the maximum level of refinement. To get rid of these gaps, the hanging nodes of the panels closest to the hull are stretched until the waterline. A comparison between a case with and without the snapping of the panels can be seen in Figure 3.2.

As far as the criterion on the curvature is concerned, the refinement is triggered if the curvature between two control points in the vertical plane exceeds a fixed value. In this way, it is possible to have a coarse representation of the incoming waves and have a finer mesh on the waves generated by the hull. A comparison between the initial time step with the hull at rest and the final one with the generated waves for a KVLCC2 in calm water can be seen in Figure 3.3. Since the method is fully nonlinear, it means that the boundary conditions have to be applied on the exact free surface location. To satisfy this requirement, the mesh generator and consequentially the refinement scheme are called at each sub-time step of the Adam-Bashforth-Moulton method.
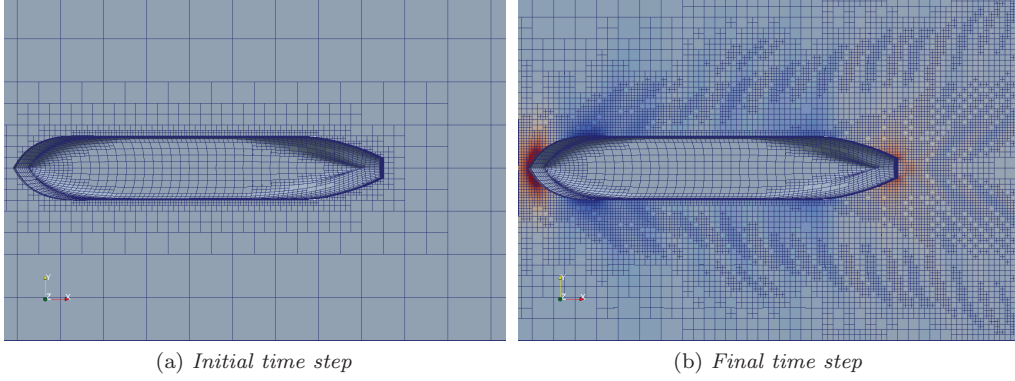
(a) *Initial time step* (b) *Final time step*

Figure 3.3: *Comparison between initial and final mesh with the adaptive mesh refinement.*

3.4   Damping zone

Since the numerical domain has a limited extension for computational reason, domain boundaries are introduced. In order to avoid unwanted reflection from the domain boundaries, a damping zone is introduced. In order to achieve that, the damping zone makes sure that the solutions from the inner and outer domain match at the intersection. The velocity potential on the outer domain known *a priori* and it represents the incoming waves. Due to the presence of a body in the inner domain, the velocity potential will be different. The purpose of the damping zone is to phase out this difference introducing a damping term in the free surface boundary conditions. The modified boundary conditions are:

$$
\begin{aligned}
\frac{D\vec{x}}{Dt} &= \nabla\phi - \nu\vec{u}_{\text{damp}} \\
\frac{D\phi}{Dt} &= -gz + \frac{1}{2}\nabla\phi \cdot \nabla\phi - \frac{p_a}{\rho} - \nu\phi_{\text{damp}}
\end{aligned}
\tag{3.7}
$$

where ν is a damping factor based on a quadratic function of the generalised space variable s:

$$
\nu(s) = \begin{cases} 0 & \text{for } s \leq s_0 \\ \mu\omega\left(\frac{s-s_0}{\lambda}\right)^2 & \text{for } s > s_0 \end{cases}
\tag{3.8}
$$

with s_0 being the beginning of the damping zone, μ is a tuning factor related to the depth and ω and λ represent the frequency and the length of the waves to be dampened. If there are irregular waves, the frequency and length of the longest one are used. Since the damping is only applied to the difference between the inner and outer potential and velocity, we have:

$$
\begin{aligned}
\vec{u}_{\text{damp}} &= \vec{u}_{\text{outer}} - \vec{u}_{\text{inner}} \\
\phi_{\text{damp}} &= \phi_{\text{outer}} - \phi_{\text{inner}}.
\end{aligned}
\tag{3.9}
$$

Note that the damping zone not only dampens out the potential due to the presence of the hull, but it helps in reducing numerical errors: while the difference between the
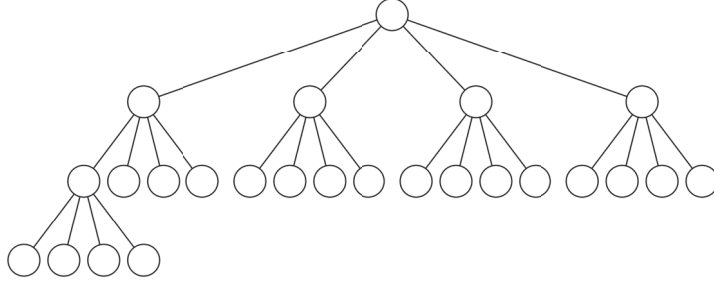
Figure 3.4: *Visual representation of Barnes-Hut grouping.*

inner and outer solution is mainly due to the disturbance of the hull, there could also be numerical effects related to discretization.

3.5 Barnes-Hut algorithm

In order to further decrease the computational effort, a Barnes-Hut algorithm, initially presented by Barnes and Hut, 1986, is implemented. Thanks to this algorithm, the computational effort needed to solve BVP is decreased from $O(n^2)$ to $O(n\log(n))$. With this algorithm, panels are grouped together in nodes based on the distance of an area of interest. A visual representation of the grouping can be seen in Figure 3.4. When the BVP is solved, the panels belonging to one node are treated as a single panel. Furthermore, the further away the node is from the point of interest, the smaller the influence of the node on it. Grouping more panels into a single node will result in a faster computation at the expenses of the accuracy. This can be controlled by the user, specifying the ratio between the dimensions of a node, *i. e.* how many panels it contains, and the distance at which the influence of the node fades away. The Barnes-Hut algorithm was initially introduced to deal with astrophysics simulations, where the influence of gravity decrease with $\frac{1}{r^2}$. Since the influence of the velocity potential varies with a $\frac{1}{r}$ function, some problems in accuracy can arise. To deal with this problem, a multipole expansion method is adopted.

3.6 Roll Damping Coefficients

In Section 2.4.1, the importance of introducing damping coefficients to account for viscosity when dealing with roll motion was presented. In this section different models for the damping coefficients and how to evaluate them will be presented. There are several ways

to represent the roll damping coefficients that are going to be used in the roll equation. The most common ones are, as can be found in Himeno, 1981:

$$B(\dot{\varphi}) = B_l\dot{\varphi} + B_q\dot{\varphi}^2 + B_c\dot{\varphi}^3$$
$$B(\dot{\varphi}) = B_l\dot{\varphi} + B_q\dot{\varphi}^2 \tag{3.10}$$
$$B(\dot{\varphi}) = B_l\dot{\varphi} + B_c\dot{\varphi}^3$$

More complex and accurate models include a dependency on the roll angle as well but they have not been considered in the current project. Historically, the quadratic formulation for roll damping has been used. Ever since the 80s, the cubic formulation started to gain more popularity because it was easier to solve numerically and analytically, as reported by Bass and Haddara, 1988.

After a damping model is chosen, the damping coefficients have to be evaluated. It is important to point out that usually, once the coefficients are evaluated, they are used for different kind of simulations and different kind of conditions. Although this might be the only approach available, the use of constant coefficients can introduce an error in simulating roll motion. An intensive campaign of simulations and results analysis on the importance of not using constant damping coefficients can be found in Contento et al., 1996. In the paper, different models including a dependence on the wave frequency and wave steepness are used showing better agreement with experimental data.

There are several techniques available to evaluate damping coefficients and in the following sections two methods that have been used for this project will be discussed. The methods available in literature to estimate damping coefficients can be divided in two categories: the methods belonging to the first group estimate the coefficients using geometrical and inertial characteristics of the ship being studied and they are generally based on regression analysis. These methods are widely used for numerical simulations since they allow to predict the coefficients without much information on the conditions which will be tested beforehand. There also are a number of methods which evaluate damping coefficients starting from model tests. The use of these methods to obtain the damping coefficients for numerical simulations find a limited applicability in a design phase, since they require model test results. On the other hand, they provide more accurate predictions since they analyse and they tune the coefficients on a specific condition: forced roll motion, roll decay or RAOs in frequency domain.

For the study presented here, a formulation proposed by Watanabe and Inoue (W-I), presented by Himeno, 1981 and simplified later on by De Kat Beck et al., 1989, was chosen as a method belonging to the first group. A Parameter Identification Technique was chosen for the second group and it will be described in the following sections.

3.6.1 Watanabe and Inoue

This very simple formulation was chosen to estimate the coefficients if no information from model tests is available. This method allows for the prediction of the quadratic term of Equation 3.10 starting from geometrical and inertial characteristics of the ship. There is also a linear term in the model but it is supposed to take into account the potential part of the damping, hence it is not evaluated since it is implicitly obtained by the code.

The main advantage of this method is that it is very simple to obtain a first guess for the damping coefficients. On the other hand, the accuracy of this prediction is not always high, especially when the ship studied is close to the limits of validity of the regression analysis. The proposed formula is:

$$B_q = h\Big[1.42\frac{C_B T}{L} + 2\frac{A_{BK}\sigma_0}{L^2} + 0.01\Big]f(Fn,\Lambda) \tag{3.11}$$

where:

$$h = \Big[\Big(\frac{KG - T/2}{B}\Big)^3 + \Big(\frac{T}{B}\Big)^2\frac{L}{4B} + \frac{cB}{64T}\Big]\frac{\rho\nabla B^2 180}{4\pi^3 C_B}$$
$$c \simeq 1.994 C_{WP}^2 - 0.1926 C_{WP} \tag{3.12}$$
$$f(Fn,\Lambda) = 1 + 0.8\frac{1 - \exp^{-10Fn}}{\Lambda^2}$$

and σ_0 and A_{bk} represent respectively the efficiency and the area of the bilge keels, where the efficiency can be obtained from a diagram as a function of the aspect ratio. L, B, T are the length, beam and draft of the ship, ∇ is the volume, C_B and C_{WP} are the block and the waterplane coefficients respectively, KG is the vertical position of the center of gravity and ρ is the density of the fluid.

3.6.2 Parameter Identification Technique

This technique obtains damping coefficients starting from model test results. It can either use time series of roll decay or frequency domain responses of roll motion, although it could be modified to include more scenarios and coupling with other motions. Similar techniques can be found in literature, the one used here was presented in Francescutto and Contento, 1999. In order to obtain the coefficients from the experimental results, the starting point is to chose an equation for roll motion expressed as sum of components, such as Equation 2.19. When the input is a time series of roll decay the model selected is:

$$I_{xx}\ddot{\varphi} = -M_{add}\ddot{\varphi} - (B_l\dot{\varphi} + B_c\dot{\varphi}^3) - (C_l\varphi + C_c\varphi^3) \tag{3.13}$$

When the input is a RAO of roll motion instead, the damping model selected is purely linear. Once the model is chosen and given some input values φ from model tests, Equation 3.13 is numerically solved using a first guess for the parameters B_l, B_c, C_l, C_c. The PIT systematically vary $\boldsymbol{p}$, a set of parameters including the ones just listed, in order to minimize the square error:

$$\chi^2(\boldsymbol{p}) = \sum_{i=1}^{N_{data}}\big(\varphi(i) - \hat{\varphi}(i,\mathbf{p})\big)^2 \tag{3.14}$$

In this way it is possible to find the best set of parameters $\mathbf{p}$ that gives the best fit between the input values φ and the numerically evaluated values $\hat{\varphi}(\mathbf{p})$. An example of the result of the fitted curve is shown in Figure 3.5.
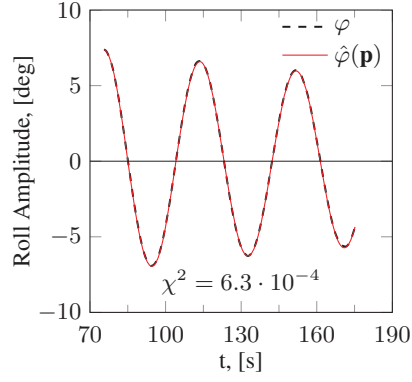
Figure 3.5: *Example of a fitted curve on the input values for a roll decay analysis using the parameter identification technique*

It is clear that this method will provide more accurate results in terms of evaluation of damping coefficient, compared to the one proposed by Watanabe and Inoue, since they will be tailored for each ship and each condition tested. On the other hand though, the main downside of this method is that the experimental results have to be available before running the simulation. Nevertheless, a good agreement with experimental data can be reached using this technique.

4 Results

In this chapter the results obtained with the potential flow method will be presented, divided into sections summarizing the four papers appended.

4.1 Summary of Paper A

In this paper, the fully nonlinear potential flow method was used to simulate roll motion. More specifically, the method was applied to two cases: roll decay for the Duisburg Test Case (DTC), a post-panamax container ship, and roll motion in regular beam waves for a Series 60 hull. Numerical simulations were compared to experimental results; a thorough description of the experimental setup can be found in el Moctar et al., 2011 for the DTC and in Bulian and Francescutto, 2013 for the Series 60.

In order to assess the quality of the simulated roll decay, the natural frequency and the equivalent linear roll damping are compared between the simulations and the experimental results. To compare the natural frequency we started from the time series of roll decay. The frequency is obtained from the time between two consecutive peaks of the same sign of the decay curve and is computed against the average value of the roll of those two peaks. In this way it is possible to obtain the variation of the natural frequency with the roll amplitude. A visual representation of the procedure is presented in Figure 4.1. To evaluate the equivalent linear damping we started from the linearized solution of the roll decay motion:

$$\varphi(t) = \varphi_0 e^{-\mu_{eq}t} \cos(\omega_0 t) \tag{4.1}$$

where φ_0 is the initial heeling angle, μ_{eq} is the equivalent linear damping and ω_0 is the natural frequency of roll motion. Similarly to what done for the frequency, we obtained the variation of the damping with the roll amplitude fitting the exponential curve passing through two consecutive peaks and plotting it against the mean roll amplitude between such peaks.
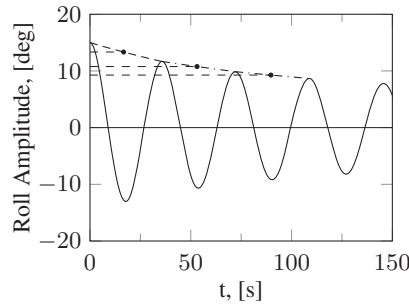

Figure 4.1: *Evaluation of natural frequency and equivalent linear damping.*
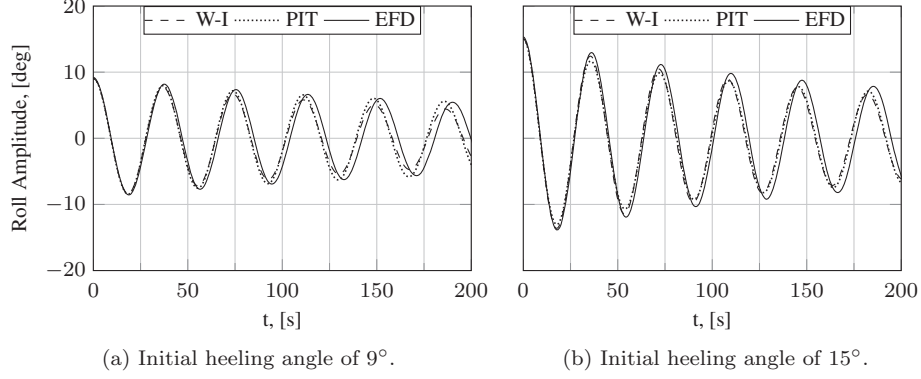
(a) Initial heeling angle of 9°. (b) Initial heeling angle of 15°.

Figure 4.2: *Time series of roll decay for the DTC.*

4.1.1 Roll Decay

Numerical simulations of roll decay were performed for the DTC for two initial heeling angles, $\varphi_0 = 9°$ and $\varphi_0 = 15°$. Both formulations to obtain the damping coefficients were used. After a comparison with experimental data, a linear term expressed as a percentage of the critical damping was added to W-I formulation. Since the roll decay curves from the experiments were available it was possible to use also the PIT to obtain the damping coefficient. With this formulation a linear plus cubic model for the damping coefficients was selected. Two different sets of values were obtained using the PIT, one for each initial heeling angle. In Figure 4.2 it is possible to see the roll decay time series of the simulations and of the experiments for both initial heeling angles.

In order to have a better term of comparison and to assess the quality of the simulations, the procedure explained at the beginning of this section is applied to obtain the variation of natural frequency and equivalent roll damping with the roll amplitude. The comparison can be seen in Figure 4.3. As can be seen, there is generally a good agreement between the simulations and the experiments. Since the damping mainly affects the amplitude of the roll decay, a good agreement was expected for the frequency, regardless of the method used to obtain the damping coefficients. In fact, the frequency is mostly affected by the restoring term and this is connected to the instantaneous wetted surface, which is properly evaluated by the method. Regarding the equivalent linear damping, there is a better agreement for the simulations were the PIT was used than for the ones using the W-I formulation. This was expected too since the coefficients obtained using the PIT are specifically suited for each condition.

4.1.2 Beam Sea

After roll decay, roll motion in beam sea was simulated. The ship used is a Series 60 hull with $C_b = 0.8$. The ship was simulated with incoming waves of different frequencies and with a constant wave steepness of $s_w = 0.01$. Experimental results for the response in beam sea were provided, as well as the backbone curve. The backbone curve represents
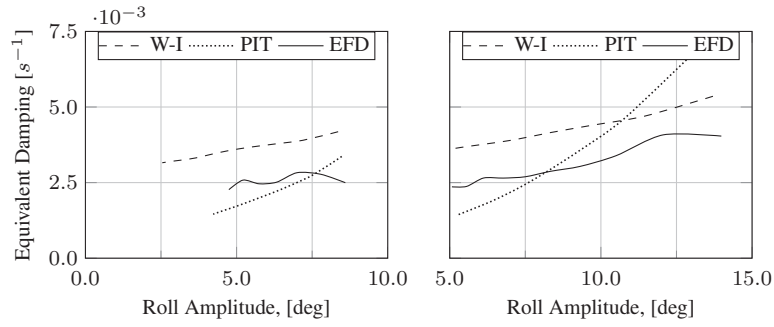
(a) Equivalent linear damping variation with an initial heeling angle of 9°.

(b) Equivalent linear damping variation with an initial heeling angle of 15°.
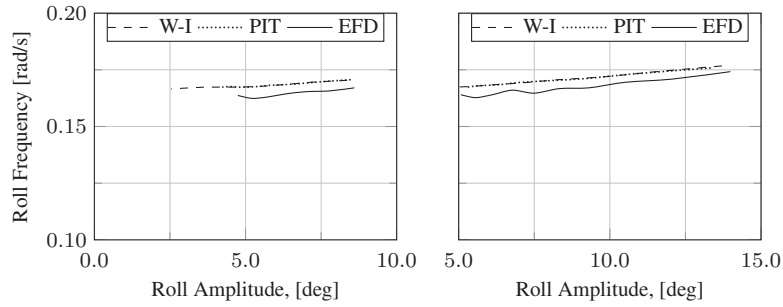
(c) Frequency variation with an initial heeling angle of 9°.

(d) Frequency variation with an initial heeling angle of 15°.

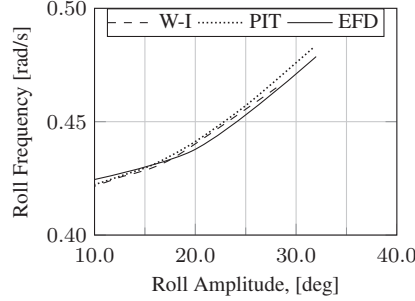Figure 4.3: *Equivalent linear damping and frequency variation.*

Figure 4.4: *Comparison of roll frequency for the S60.*

the variation of the natural frequency with roll amplitude and it was used to verify that the simulations were able to evaluate the roll natural frequency properly. In order to verify this, roll decay simulations were performed and the result, in terms of natural frequency, can be seen in Figure 4.4. Both formulations to obtain the damping coefficients were used. Initially for the beam sea as well a linear term expressed as a percentage of the critical damping was added for the W-I formulation. Since only beam sea experimental results were available, the coefficients from the PIT were obtained analyzing the response in frequency domain. The model chosen for this is a purely linear one.

In Figure 4.5 it is possible to see the RAOs of roll motion in beam sea. As expected, the results obtained using the PIT match considerably better the experimental results. Not only the points in the RAO but also the backbone curve is in better agreement when the PIT is used. In Figure 4.6 the RAO is presented for the simulations not including the linear term in the W-I formulation. There is an improvement in the results but the PIT proved to perform better in the evaluation of the damping coefficients.

4.1.3 Conclusions

In paper A roll decay and roll motion in beam sea were simulated using the two techniques presented in Section 3.6 to obtain the damping coefficients. As far as roll decay is concerned, a general good agreement was found regardless of the method used to obtain the coefficients, although a better match with experimental results is achieved with the PIT. For beam sea instead, a good agreement can be achieved only if a proper method is used to get the coefficients: the W-I formulation did not give satisfactory results. This could be related to various reasons. First of all, roll decay is a much simpler phenomenon compared to beam sea. Furthermore, the W-I method is based on a regression analysis and could therefore be too simplistic for some cases. In paper A, it was possible to show that if a proper formulation for the damping coefficients is used, it is possible to achieve satisfactory results.
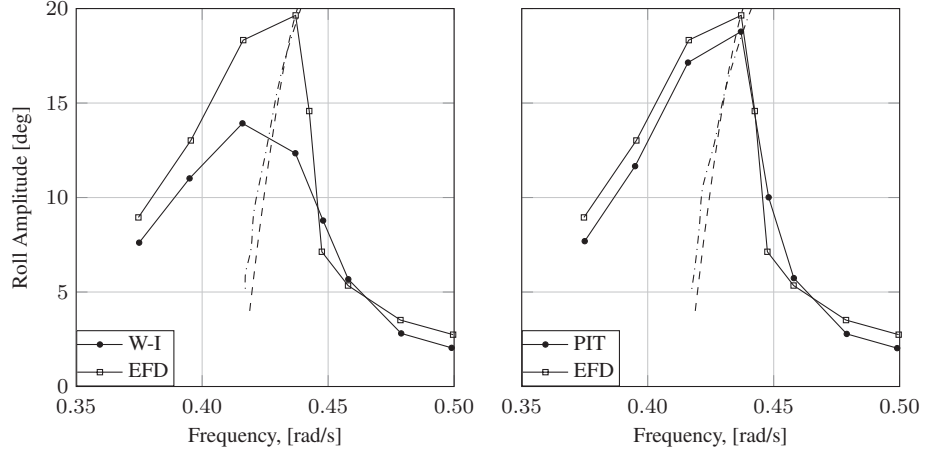
(a) Beam sea response with W-I formulation. (b) Beam sea response with PIT formulation.

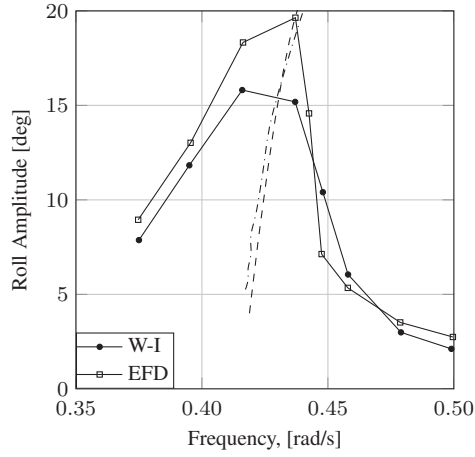Figure 4.5: *Beam sea results with constant wave steepness $s_w = 1/100$.*

Figure 4.6: *S60 beam sea response using only the quadratic term of W-I formulation.*

4.2 Summary of Paper B

In this paper, the potential flow method was used to replicate SAFEDOR, an EU benchmark study aimed at assessing the capabilities of existing numerical methods to evaluate parametric rolling. In the benchmark, presented in Papanikolaou and Spanos, 2009, numerical simulations were compared with model test results for a container ship sailing in head and following waves. Two different loading conditions were investigated and model tests were carried out for monochromatic, three components and irregular waves. The benchmark had two main goals: the first was to assess the capabilities of the tested codes to capture the occurrence of parametric rolling. The second was to compare the simulated roll amplitudes with the ones from model tests, *i. e.* the quality of the simulations. In paper B the benchmark was replicated using the potential flow method and both formulations to obtain the damping coefficients were used.

Given the diversity of the incoming waves, different responses were expected. In order to make the comparison of the different methods possible, a single value of the response had to be taken. In the case of a reached steady state of the response, which is typically the case for monochromatic waves, the mean value of the amplitude of the stationary response was taken. A typical response for monochromatic waves can be seen in Figure 4.7a. For three components and for irregular waves a steady state of the response was not achieved and typical responses can be seen in Figures 4.7b and 4.7c respectively. Therefore for the comparison the average value of the amplitude of the roll motion was used, excluding the transient part where the motion was still developing.

In order to verify whether the methods were able to predict the occurrence of parametric rolling, regardless of the amplitude of the motion predicted, a success rate was introduced in the study. To define the success rate, a critical roll amplitude is used to compare simulations with experiments. Four values of critical roll amplitude are used: $\varphi_{cr} = 0.5°, 1.0°, 1.5°, 2.0°$. An $i-th$ event is classified as successful when the simulated φ_i and experimental $\overline{\varphi}_i$ values of the roll motion are the same with respect of the critical value. The success rate over the n cases is defined as:

$$P = \frac{1}{n}\sum_{i=1}^{n} q_i \tag{4.2}$$

where:

$$q_i = \begin{cases} 1 & \text{if } (\varphi_i - \varphi_{cr})(\overline{\varphi}_i - \varphi_{cr}) \geq 0 \\ 0 & \text{if } (\varphi_i - \varphi_{cr})(\overline{\varphi}_i - \varphi_{cr}) < 0 \end{cases} \tag{4.3}$$

To assess the quality of the predicted amplitude, standard deviation σ and correlation coefficient r were used in the benchmark. Being $\widehat{\varphi}_i = \varphi_i - \overline{\varphi}_i$ the difference between the simulated and experimental results for the $i-th$ case and $\widehat{\varphi}_m$ the average of the differences in the response between simulations and experiments for all conditions,σ and
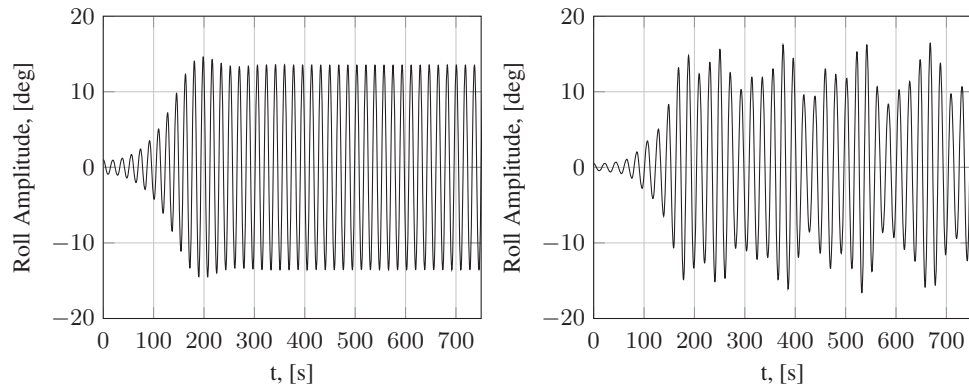
(a) Response with monochromatic waves.

(b) Response with three components waves.
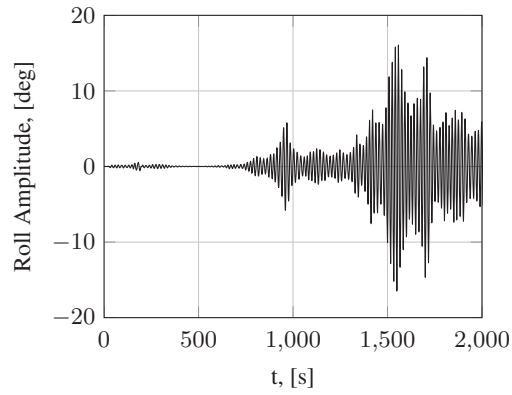
(c) Response with irregular waves.

Figure 4.7: *Different responses of parametric rolling.*

Figure 4.8: *Roll decay for the case with $\overline{GM} = 1.38\,m$.*

r are evaluate as:

$$\sigma = \sqrt{\frac{\sum_{i=1}^{n}(\widehat{\varphi}_i - \widehat{\varphi}_m)^2}{n-1}} \qquad (4.4)$$

$$r = \frac{cov(\varphi, \overline{\varphi})}{\sigma_\varphi \sigma_{\overline{\varphi}}} \qquad (4.5)$$
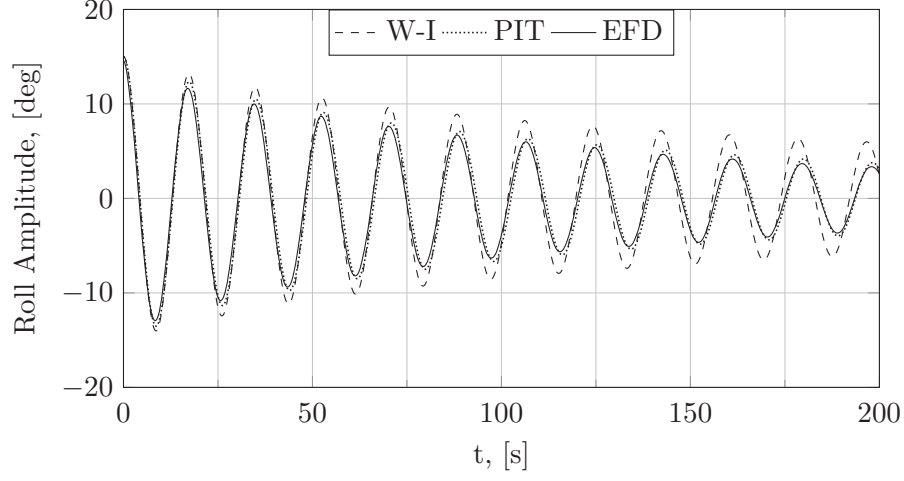
4.2.1 Numerical Simulations

For the benchmark, semi-captive model tests of a container ship were carried out in different wave systems. A total number of 22 cases were tested with different heading angle χ and can be seen in Table 4.1. Irregular waves were obtained using a JONSWAP spectrum with an overshoot parameter $\gamma = 3.3$. Cases 1 and 12 are roll decay tests and they were used to tune the inertia characteristics and the damping coefficients. The only difference between the two loading conditions is the vertical position of the center of gravity. For the numerical simulations presented here, only Case 1 was available. Therefore, the damping coefficients using the PIT were available only for the first loading condition, which was used for cases $01 \div 11$. On the other hand, the W-I formulation was used for all cases. In Figure 4.8 the roll decay simulations are compared with experiment for case 1. As can be seen, a good agreement is reached between computations and experiments, especially in terms of frequency. The simulation using the coefficients obtained with the PIT matches well the amplitudes too.

In Figures 4.9 and 4.10, the amplitudes of the parametric roll for each case are shown and compared with the experimental results. As mentioned earlier, for the cases $12 \div 22$ only the damping coefficients obtained using the W-I method were used. Since it is not easy to evaluate the quality of the simulations based purely on these two figures,

Table 4.1: Experiments conditions

| ID	GM	χ	Fn	H_1	T_1	H_2	T_2	H_3	T_3	Description
01	1.38	-	0.00	-	-	-	-	-	-	Roll Decay
02	1.38	180°	0.08	3.6	10.63	-	-	-	-	1 Harmonic
03	1.38	180°	0.08	5.7	10.63	-	-	-	-	1 Harmonic
04	1.38	180°	0.12	3.6	10.63	-	-	-	-	1 Harmonic
05	1.38	180°	0.12	5.7	10.63	-	-	-	-	1 Harmonic
06	1.38	180°	0.12	2.4	10.63	2.4	9.66	2.4	11.55	3 Harmonics
07	1.38	180°	0.12	4.0	10.63	1.0	9.66	1.0	11.55	3 Harmonics
08	1.38	180°	0.12	5.0	10.63	-	-	-	-	Irregular
09	1.38	160°	0.12	3.6	10.63	-	-	-	-	1 Harmonic
10	1.38	160°	0.12	5.7	10.63	-	-	-	-	1 Harmonic
11	1.38	160°	0.12	4.0	10.63	1.0	9.66	1.0	11.55	3 Harmonics
12	1.00	-	0.00	-	-	-	-	-	-	Roll Decay
13	1.00	0°	0.08	3.6	8.00	-	-	-	-	1 Harmonic
14	1.00	0°	0.08	6.0	8.00	-	-	-	-	1 Harmonic
15	1.00	0°	0.04	3.6	8.00	-	-	-	-	1 Harmonic
16	1.00	0°	0.04	6.0	8.00	-	-	-	-	1 Harmonic
17	1.00	0°	0.04	2.4	8.00	2.4	7.11	2.4	8.89	3 Harmonics
18	1.00	0°	0.08	2.4	8.00	2.4	7.11	2.4	8.89	3 Harmonics
19	1.00	0°	0.08	5.0	8.00	-	-	-	-	Irregular
20	1.00	180°	0.08	5.0	12.12	-	-	-	-	1 Harmonic
21	1.00	180°	0.12	5.0	12.12	-	-	-	-	1 Harmonic
22	1.00	180°	0.08	4.0	12.12	1.0	10.77	1.0	13.47	3 Harmonics
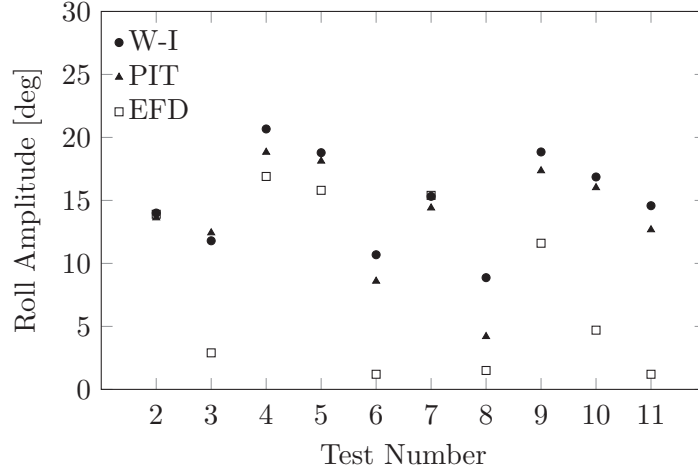
Figure 4.9: *Mean roll amplitudes for the cases with* $\overline{GM} = 1.38\,m$.

Table 4.2: Correlation coefficient and standard deviation.

	σ	r
PIT tests $2 \div 11$	$4.64°$	0.74
W-I tests $2 \div 11$	$4.71°$	0.74
W-I tests $13 \div 22$	$6.63°$	0.67
W-I tests $2 \div 22$	$6.13°$	0.62
Overall	$10.5°$	0.37
Best Performing	$6.4°$	0.64

the success rate and the standard deviation were evaluated. In Table 4.2 the standard deviation and correlation coefficient are presented and compared with the values from the benchmark. As can be seen, a good agreement with experimental results is achieved. In the benchmark, the mean values of standard deviation and correlation coefficient for all methods were calculated as well as the values for the four best performing ones. They are both presented in the table. As can be seen, the simulated parametric roll is aligned with the best performing methods. In Table 4.3 the success rate of the simulations is compared with the ones from the benchmark. The success rate from the simulation is also aligned with the best performing methods from the benchmark.

4.2.2 Conclusions

In the paper, numerical simulations of parametric roll were compared with a benchmark study were different numerical methods were evaluated. To compare the current method with the results presented in the benchmark success rate, standard deviation and cor-
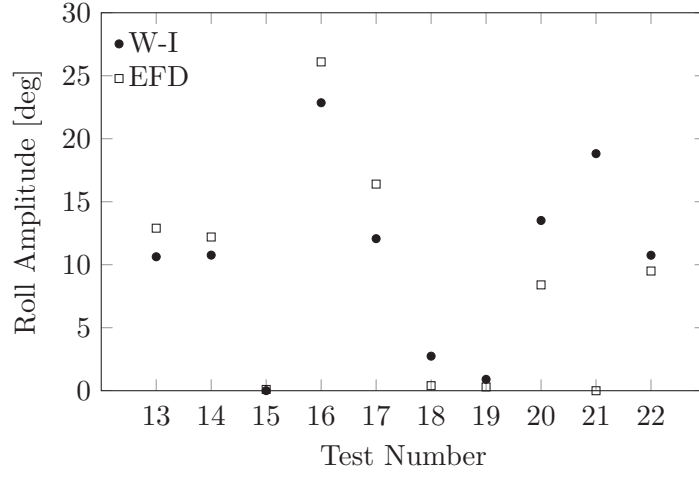
Figure 4.10: *Mean roll amplitudes for the cases with $\overline{GM} = 1.0\,m$.*

Table 4.3: Success rate as a function of the critical rolling angle.

	$P|_{x_{cr}=0.5°}$	$P|_{x_{cr}=1.0°}$	$P|_{x_{cr}1.5°}$	$P|_{x_{cr}=2.0°}$	P_m
PIT tests $2 \div 11$	1.0	1.0	0.7	0.7	0.85
W-I tests $2 \div 11$	1.0	1.0	0.7	0.7	0.85
W-I tests $13 \div 22$	0.7	0.8	0.8	0.8	0.78
W-I tests $2 \div 22$	0.85	0.9	0.75	0.75	0.81
Overall	*na*	*na*	*na*	*na*	0.62
Best Performing	*na*	*na*	*na*	*na*	0.78

relation coefficient were used. The success rate represents the accuracy of a method to successfully predict the occurrence of the parametric roll. Based on the cases tested, we can expect a correct prediction eight times out of ten. Furthermore, the success rate was also obtained separately for the two loading conditions, showing similar results. This suggests that the accuracy of the prediction does not depend on the loading condition. Not only, the success rate is the same regardless of the technique used to obtain the damping coefficients, where both formulations were used.

As far as the quality of the predicted amplitude is concerned, standard deviation and correlation coefficient show a good agreement between the simulations and the experimental results. The quality of the simulations is again aligned with the best performing methods from the benchmark. The difference between σ and r for the tests $2 \div 11$ and $13 \div 22$ is related to a significance difference in amplitude in the test number 21, as can be seen in Figure 4.10, where no roll motion was measured in the experiments and the simulated condition has an amplitude around $\phi \cong 19°$. However, the ratio between encounter and natural roll frequencies is $\omega_e/\omega_\phi = 2.13$. One of the conditions that triggers parametric rolling is that such ratio has to be in the range of $\omega_e/\omega_\phi \cong 2/n$ with n integer. It can be said then that this case lays on the edge of possible parametric rolling. From a design point of view though, the current method is on the safe side since it would show a possible danger situation when conditions are on the borderline.

4.3 Summary of Paper C

In this paper, the numerical method is used to replicate a benchmark case of lightering operation in confined waters. A lightering operation consists of transferring cargo to one ship to another while the two are sailing close to each other at the same speed. Once the transferring is complete, the *service ship*, the one which received the cargo, overtakes the other. When the two ships are sailing close to each other, there are hydrodynamic interactions which lead to unbalanced pressures between starboard and portside. This unbalance can lead to attraction forces which can cause a collision. In the paper, forces and moments are compared with captive model tests results available in Lataire et al., 2009. Results were also compared with numerical simulations obtained using SHIPFLOW viscous solver and presented in Zou and Larsson, 2013.

In the simulations a *Ship To Be Lightered* (STBL) and a *Service Ship* (SS) sail at the same speed and at different transversal positions. The ships are tested at various combinations of drafts and water depth as well as various speeds. The midship sections of the two ships are aligned in all cases tested here. The STBL is a model scale of the KVLCC2 and the SS is an Aframax tanker. Both ships were equipped with rudder and propeller during the experiments but in the numerical simulations presented here, rudder and propeller are not taken into consideration and the ships are towed at the prescribed speed. A description of the conditions is presented in Table 4.4. In the table, d is the water depth and δy is the distance between the ships sides.

Forces and moments are measured in each ship's coordinate system. The quantities measured are: longitudinal force X, lateral force Y and yaw moment N. Since the potential flow does not take into account viscosity, frictional resistance is taken into account using the *ITTC '57* line.

4.3.1 Numerical Results

The time series of the forces and moments have to be processed before comparing the results with the experimental values. The time series for case B can be seen in Figure 4.11. A *Double Exponential Smoothing* (DES) is applied on the time series of the forces

Table 4.4: Main parameters of benchmark cases.

-	A	B	C
T_{STBL} [m]	12.825	12.825	12.825
T_{SS} [m]	7.5	15.0	15.0
d [m]	17.250	20.250	36.625
v [kn]	6.0	5.0	4.0
δy [m]	50.0	50.0	4.0

and moments:

$$\begin{cases} F_{DES,t} = \alpha F_t + (1-\alpha)F_{DES,t-1} \\ F_{DES,t}^d = \alpha F_{DES,t} + (1-\alpha)F_{DES,t-1}^d \end{cases} \tag{4.6}$$

where F_t is the value of the force at the time t, $F_{DES,t}$ the value of the the first exponential smoothing, $F_{DES,t}^d$ the double smoothing and α is the smoothing factor. As can be seen from Figure 4.11, a smoothing technique was necessary to evaluate the attraction forces and the yaw moments.

The comparison of the forces and moments evaluated is presented in Figure 4.12, where *SFLM* stands for SHIPFLOW MOTIONS, *SFLR* for SHIPFLOW Ranse solver and *EFD* for experimental results. A good agreement is reached for the attraction forces, while the forces along the $x-$axis have different behaviours depending of the hull: the forces for the Aframax tanker are properly evaluated while there are some discrepancies for the KVLCC2. There are some limitations in the methods used that must be pointed out: the potential flow does not include viscous resistance. To account for this, the frictional resistance evaluate using the ITTC '57 line is implemented. The formulation does not include the form factor. On the other hand, the viscous solver uses a double model, *i.e.* symmetry-plane at the free surface. In addition to this, the wave resistance is very small compared to the viscous part for all the cases since the Froude numbers are in the range $Fn = 0.037 \div 0.055$. Furthermore, for such low Froude numbers, a high number of waves is expected to be generated by the hull. The grid resolution required to capture all the waves is too high. Among all the results, the ones which seem to be the hardest to evaluate properly are the yaw moments. The most extreme case is visible for the Aframax tanker, where an opposite sign is obtained with the potential flow compared to experiments and simulations with the viscous solver. A wrong sign is obtained for case A for the KVLCC2 as well, although the same issue was experienced with the viscous solver. There are two possible causes that can lead to this error. First of all, the pressure recovery at the stern can be considerably higher with a potential flow solver than with a viscous solver because of no separation. The net force and moment resulting from this will be different in magnitude. Furthermore, the center of the resultant force will be shifted from the one obtained with a viscous solver and a difference in the sign of the moment could arise. Second of all, since these cases are asymmetrical, there will be a circulation acting on the hull, resulting in a lift force. The circulation is not captured by a potential flow using only sources distribution on the panels. The same problem was faced and discussed in other papers where potential flow methods were used to evaluate the yaw moment, see for instance Yuan and Yeung, 2018.

4.3.2 Conclusions

In the paper, a lightering operation was replicated. Forces and moments were compared with both experimental results and with values obtained with viscous computations. As shown in the previous section, forces are captured fairly well, both in magnitude and in direction. Particularly good agreement is reached for the attraction force deriving from the hydrodynamic interaction. There are some issues for the evaluation of the longitudinal forces though, since with such a low speed a correct prediction of the wave resistance can be a source of uncertainties with a potential flow code. Increasing further
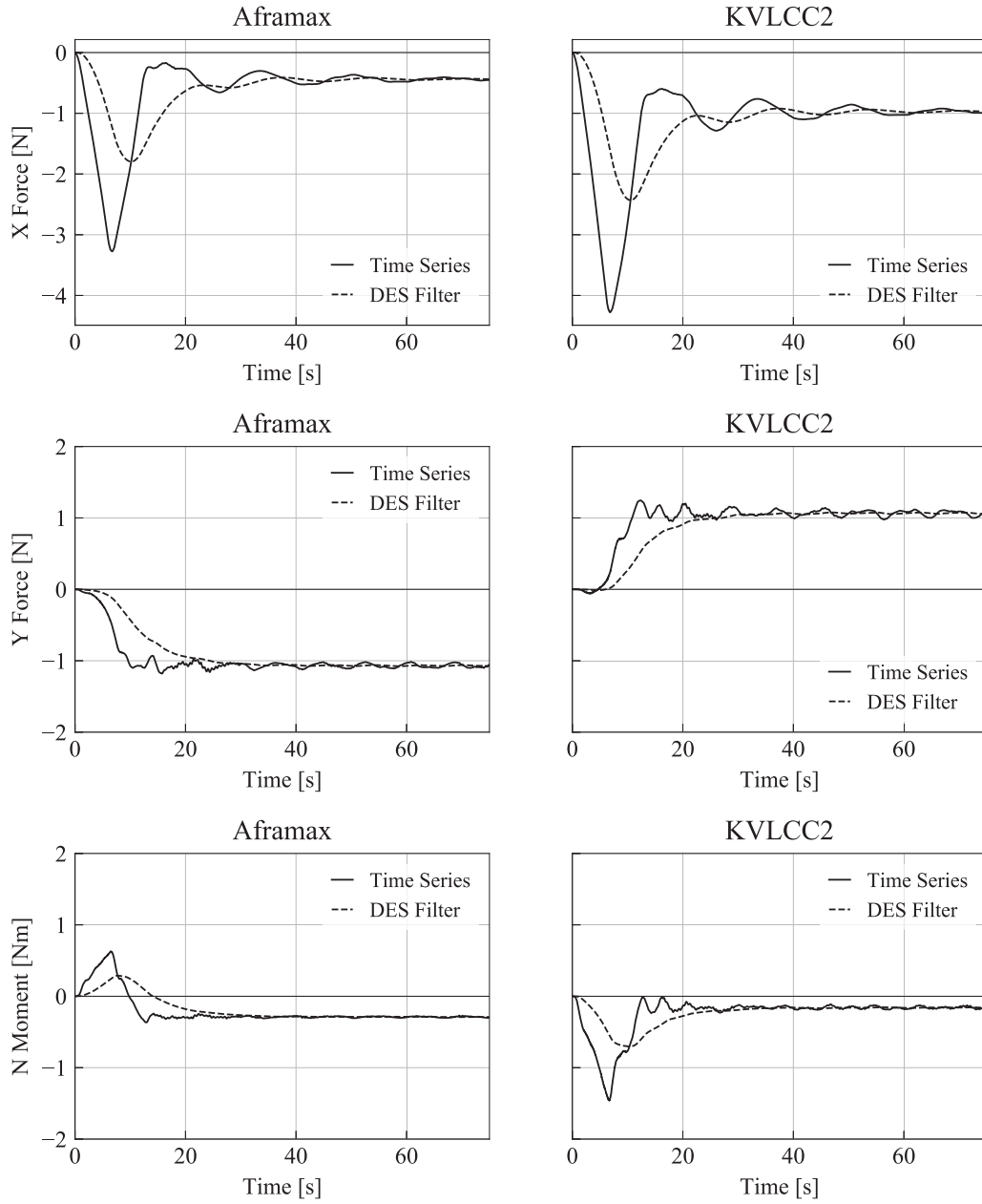
37

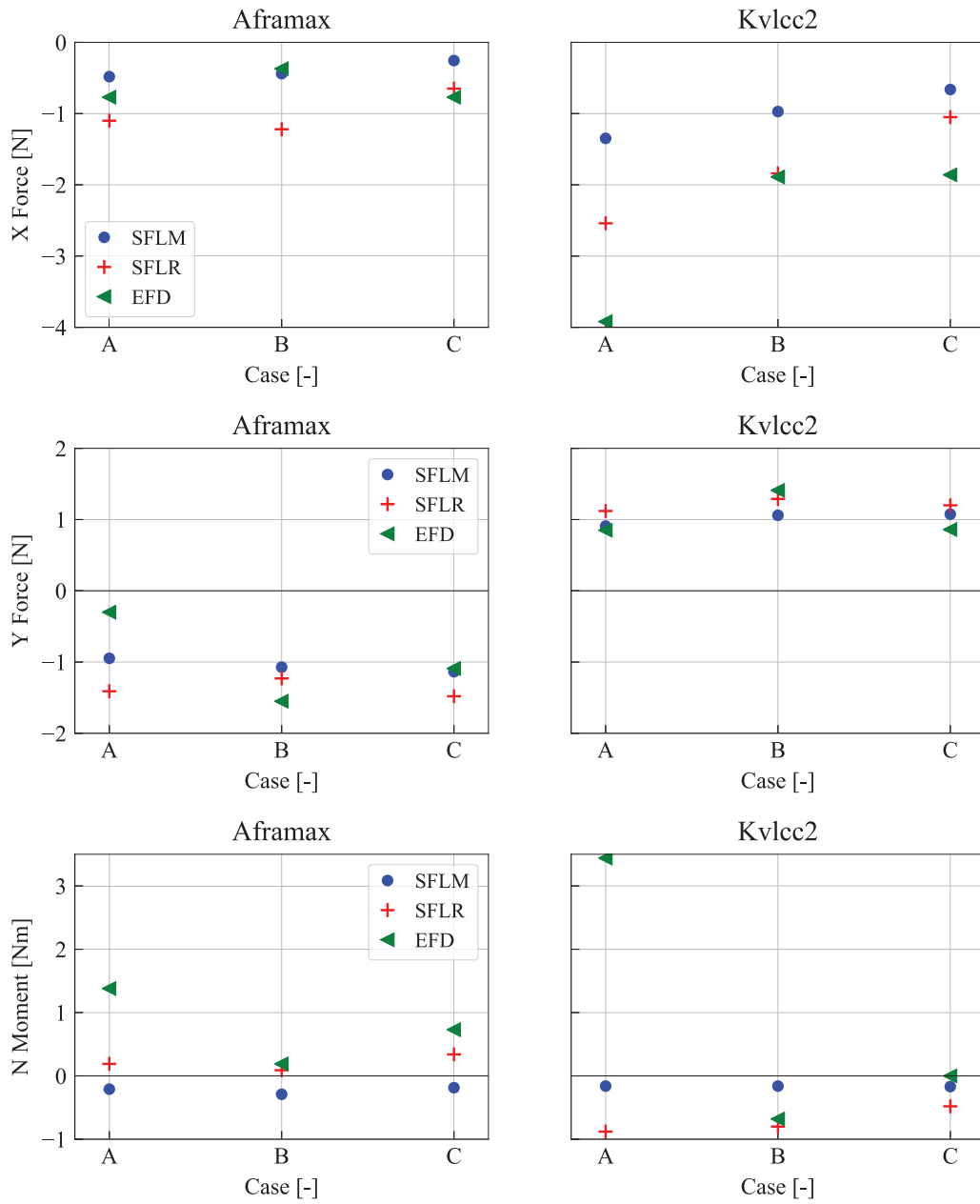Figure 4.11: *Time series of the forces and moments for case B.*

Figure 4.12: *Comparison between forces and moments.*

the grid resolution of the free surface between the hulls and downstream, could partially solve this issue. It must be stressed again that for these cases the viscous resistance is the predominant component, so it is not possible to achieve a perfect match with experimental results using a potential flow method. As far as the evaluation of the moments is concerned, further investigation is needed. Because of the higher pressure in the stern obtained with potential flow, an error will be introduced. Modeling of the lift forces would help to account for the effects from crossflow and circulation.

4.4 Summary of Paper D

In this paper numerical simulations of added resistance in head waves of the KVLCC2 hull were carried out and compared with experimental results. A correct estimation of added resistance during a design phase has becoming more and more important. The International Maritime Organization (IMO) has introduced new rules to address energy efficiency in the shipping industry in order to reduce CO_2 emissions. One of the most important aspects of these new rules is the evaluation of the Energy Efficiency Design Index (EEDI), which represents the carbon dioxide produced per ship's capacity mile. To obtain a reliable value of the EEDI, it is important to estimate the added resistance of the ship in the actual operation scenario.

Before comparing the numerical results with the experimental data and other methods available in literature, a grid dependency study was performed. The influence of different timestep sizes was also investigated. The numerical domain is fixed for all different grids tested and is set equal to $3L_{pp}$ upstream and $3L_{pp}$ downstream from the centerplane of the ship and for $2L_{pp}$ sideways. The incoming waves range from $\lambda = 0.4 \cdot L_{pp}$ to $\lambda = 1.4 \cdot L_{pp}$. The wave steepness is set according the one used in the experiments and is equal to $s_w = 1/50$ for $\lambda \leq 0.9$ and $s_w = 1/100$ for $0.9 < \lambda \leq 1.4$. The length of the simulations is set in order to achieve a convergence in the forces and is kept equal between the different conditions. The number of encounter periods goes from a maximum of 100 for $\lambda = 0.4 \cdot L_{pp}$ to a minimum of 44 for $\lambda = 1.4 \cdot L_{pp}$.

4.4.1 Grid Dependency

A grid dependency study had been carried out to find the best compromise between accuracy and computational time. This study focused on the mesh resolution on the free surface. The mesh on the hull is fixed and kept constant between all the different cases tested. As mentioned in Section 3.3.2, the mesh on the hull has a higher resolution along the waterline and on areas where there is a high curvature and flare. The total number of panels used to discretize the hull is approximately 5.3k.

Both criteria that trigger the refinement for the free surface were analyzed separately, in order to find their impact on the solution. In Table 4.5, all the different cases tested is presented. For group a, cases 1, 2 and 3, the same maximum level of refinement is kept on the intersection between the free surface and the hull and on the curvature of the free surface. For group b, cases 4, 5 and 6, only the maximum level on the curvature is varied. In this way it is possible to study how the resolution of the generated waves affects the solution, since the mesh around the hull does not vary. For group c, cases 7, 8 and 9, the initial base grid is changed. For the other cases the level zero refinement corresponded to 36 panels along the x-axis and 12 along the y-axis. For these last set of simulations the base grid is changed in order to have the area of the initial panels half and double compared to other cases. Note that cases 3, 6 and 8 are the same. In the table it is also possible to see the initial and final number of panels on the free surface in calm water and the number of panel along the waterline (WL). The number of panels per fundamental wave length are also reported in the table, both along the waterline and on a longitudinal wave cut at $y = 0.15 \cdot L_{pp}$.

Table 4.5: Levels

		Levels		Panels Calm Water			Panels per wave	
	ID	WL	Curv.	Initial	Final	WL	@ WL	@ $y = 0.15 L_{pp}$
a	1	4	4	580	1100	50	6.4	10.7
	2	5	5	715	2700	95	12.1	20.2
	3	6	6	1255	5900	190	24.2	29.1
b	4	6	4	1255	1760	190	24.2	11.2
	5	6	5	1255	3200	190	24.2	20.7
	6	6	6	1255	5900	190	24.2	29.1
c	7	6	6	745	3750	135	17.2	26.2
	8	6	6	1255	5900	190	24.2	29.1
	9	6	6	1680	8000	270	34.4	32.5

(a) *Wave length $\lambda = 0.6 \cdot L_{pp}$*   (b) *Wave length $\lambda = 1.0 \cdot L_{pp}$*   (c) *Wave length $\lambda = 1.2 \cdot L_{pp}$*
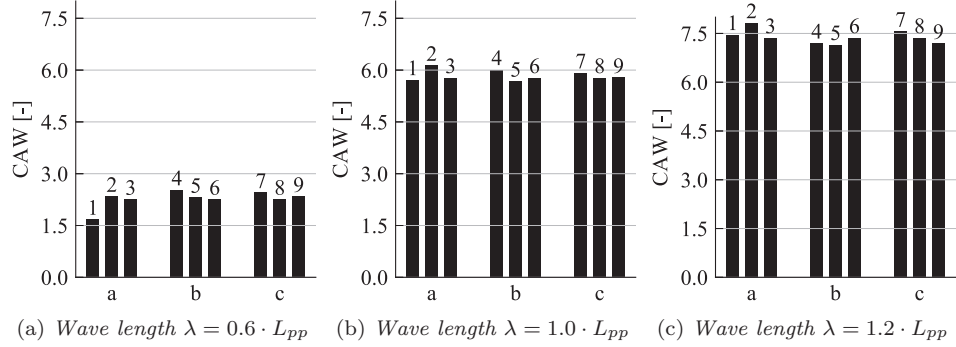
Figure 4.13: *Variation of added resistance coefficient for the different cases for three wave lengths.*

In order to compare the different grid resolutions, the different grid were tested with incoming waves. To find a convergence, added resistance coefficient and nondimensional heave and pitch were compared for three wave lengths: $\lambda = (0.6, 1.0, 1.2) \cdot L_{pp}$. The results are presented in Figures 4.13, 4.14 and 4.15 respectively. As can be observed, the variations for the motions are quite limited, while there are bigger discrepancies for the added resistance. The bigger discrepancies can be observed for cases 1, 2 and 4 where there are not enough panels around the waterline to properly evaluate the forces acting on the hull.

Another important aspect in the selection was to compare the different computational time needed for the simulations. The computations were run on 4 cores on an Intel i7-7700K CPU @ 4.20 GHz and the time needed for the all the cases are reported in Table 4.6 for two wave lengths. In the table the computational time per wave encounter is also presented. This value represents an average: it is obtained dividing the total computational time with the number of encounter periods. Since case 4 was run on
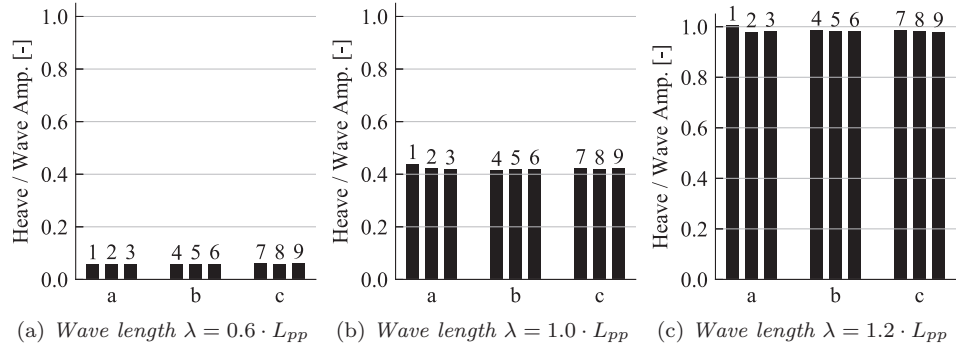
(a) *Wave length* $\lambda = 0.6 \cdot L_{pp}$ (b) *Wave length* $\lambda = 1.0 \cdot L_{pp}$ (c) *Wave length* $\lambda = 1.2 \cdot L_{pp}$

Figure 4.14: *Variation of heave for the different cases for three wave lengths.*

(a) *Wave length* $\lambda = 0.6 \cdot L_{pp}$ (b) *Wave length* $\lambda = 1.0 \cdot L_{pp}$ (c) *Wave length* $\lambda = 1.2 \cdot L_{pp}$
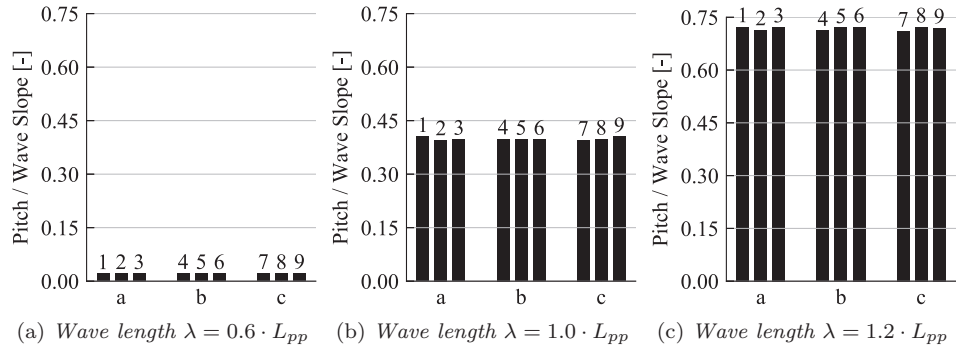
Figure 4.15: *Variation of pitch for the different cases for three wave lengths.*

Table 4.6: Computational time for different cases

	ID	$\lambda = 0.6$		$\lambda = 1.2$	
		T	T per T_e	T	T per T_e
	1	6h35'	5.2'	6h50'	8.4'
a	2	14h	11.1'	14h30'	17.8'
	3	37h20'	29.5'	41h	50.2'
	4	na	na	na	na
b	5	19h15'	15.2'	19h15'	23.6'
	6	37h20'	29.5'	41h	50.2'
	7	20h20'	16.1	20h50'	25.5'
c	8	37h20'	29.5'	41h	50.2'
	9	68h	38.2'	94h	101.6'

another machine, it is not reported in the table.

Comparing the results from the forces with the ones from the computational time, we could see that the best cases were the IDs 5 and 7. Increasing the mesh resolution further from these cases, resulted in a very high computational demand. To chose between cases 5 and 7, we looked at contour plots and at the longitudinal wave cut, shown in the appended paper, and compared them with case 8, which represent a finer resolution. While the forces are very similar for both cases 5 and 7, the wave system is slightly better captured by case 7 and the wave cut is closer to the one obtained from case 8. For these reasons, we decided to use case 7 to compare the results with the experiments.

4.4.2 Time Step Dependency

Before proceeding to the comparison with experiments and other methods, it was observed that a further investigation was needed for short waves. To assess the problem, the influence of the time step size on the solution was investigated. During the simulations, the time step size is based on the period of the fundamental wave generated by the ship, with wave length $\lambda = 2\pi Fn^2 L$. For the grid comparison the time step was set in order to have 30 time steps per fundamental wave period. For this investigation, three more values were chosen: 15, 45 and 60 steps. Varying the number of time steps per fundamental wave period will affect the number of time steps per encounter period, as can be seen in Table 4.7. The added resistance coefficient for the four different cases can be seen in Figure 4.16.

As can be seen from Figure 4.16 there is a clear convergence increasing the number of time steps. As reported in Seo et al., 2014, in short waves nonlinearities play an important role in the evaluation of added resistance. Since the code used here assumes fully nonlinear boundary conditions and the forces are obtained from the direct integration of the nonlinear pressure on the hull surface, the discrepancies in the short waves range could be mainly due to an insufficient number of time steps for these cases, as can be seen in Table 4.7. The case selected for the comparison with experiments and other methods

Table 4.7: Number of time steps per encounter period for the different cases.

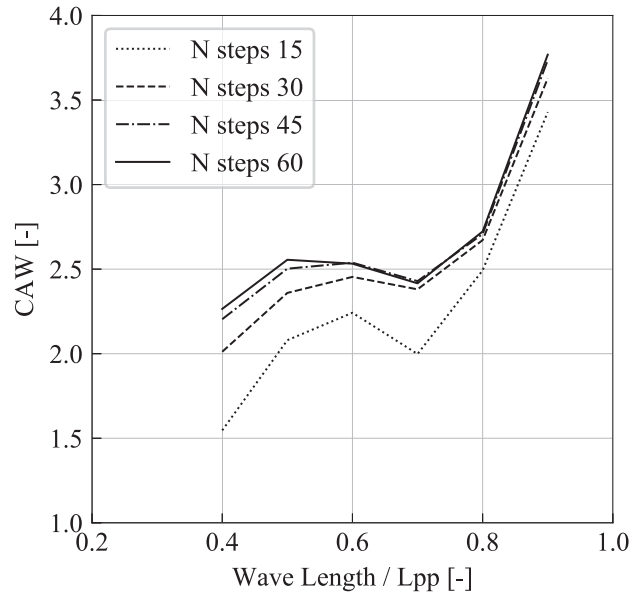|	time steps per T_e			
λ/L	N steps 15	N steps 30	N steps 45	N steps 60
0.4	18	35	53	71
0.5	21	41	62	82
0.6	23	47	70	93
0.7	26	51	77	103
0.8	28	56	84	112
0.9	30	60	91	121
1.0	32	65	97	129
1.1	34	69	103	137
1.2	36	73	109	145
1.3	38	76	114	152
1.4	40	80	120	160

Figure 4.16: *Added resistance coefficient for different number of time steps per fundamental wave.*
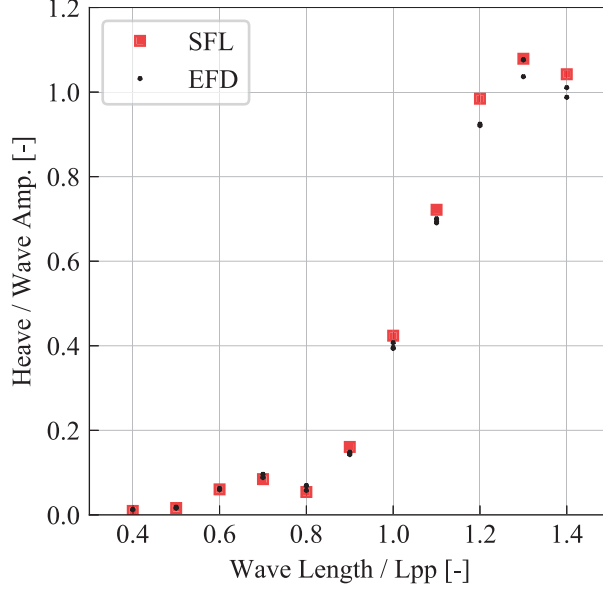
Figure 4.17: *Non-dimensional heave for case 7.*

is the one with 45 time steps per fundamental wave period.

4.4.3 Results

In Figures 4.17 and 4.18 the comparison for heave and pitch is shown. Simulated heave and pitch match extremely well the experimental data in the small waves range. For longer waves, a very good agreement can still be seen although heave and pitch are slightly overpredicted.

In Figure 4.19 it is possible to see the comparison between the simulated added resistance coefficient from the current fully nonlinear potential flow and the ones obtained with model tests and from other simulations available in literature. The other methods used for comparison are: a linear potential flow presented in Hizir et al., 2019, a partially nonlinear potential flow method and an Euler method presented in Seo et al., 2014 and an URANS method presented in Sadat-Hosseini et al., 2013. As can be seen, except for the linear potential flow method, there is a general good agreement between the current work and the other computations and the model test results, especially for waves longer than $\lambda = 1.0 \cdot L_{pp}$. For short waves, there is a higher scatter in the results. Since the forces in waves are closer in value to the one obtained in calm water, even a small difference will results in a bigger discrepancy in the added resistance coefficient. It must be pointed out also that the wave steepness for the present method was the same as in the experiments ($s_w = 1/50$ for $\lambda \leq 0.9$ and $s_w = 1/100$ for $0.9 < \lambda \leq 1.4$), while the steepness for the other methods was $s_w = 1/60$ for the linear potential flow, $s_w = 1/40$ for the partially nonlinear potential flow and Euler method and $s_w = 1/53$ for the URANS method.
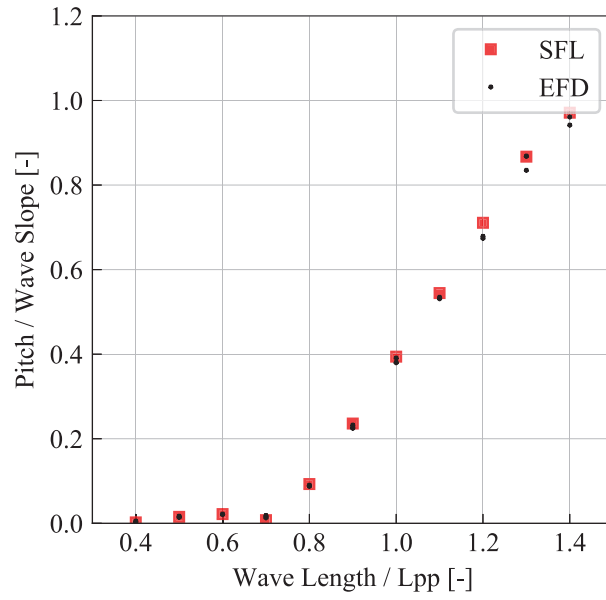
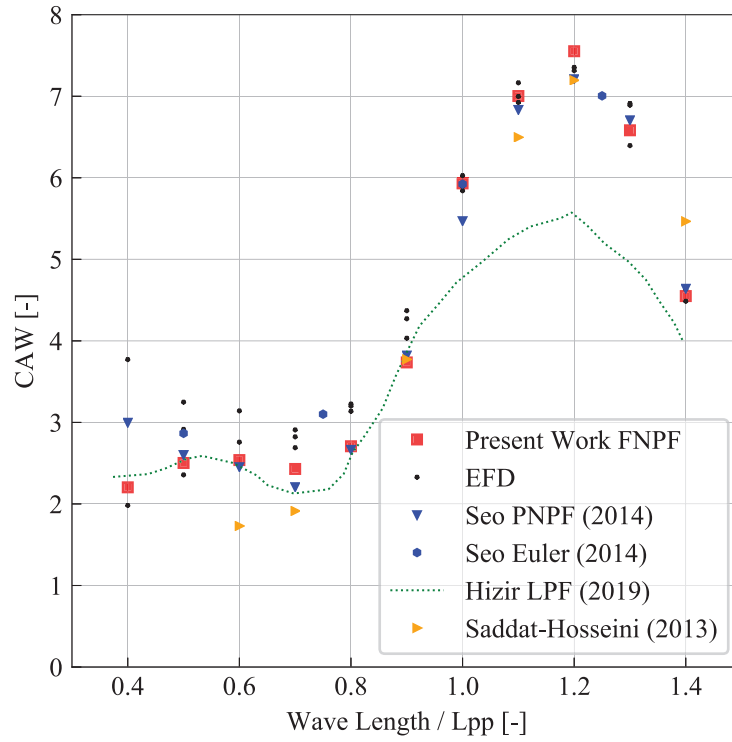Figure 4.18: *Non-dimensional pitch for case 7.*

Figure 4.19: *Added resistance coefficient for case 7.*

47

4.4.4 Conclusions

The numerical results for heave and pitch match very well with the experimental data for all wave lengths. The added resistance coefficient was compared with experimental results and with other numerical methods, including linear potential, partially nonlinear potential flow, Euler method and URANS, and a general good agreement is found. For shorter waves there is a bigger discrepancy but the added resistance is still comparable to experimental results and to other methods. For this range, even a small deviation in the estimation of the force could lead to bigger differences in terms of added resistance coefficient. Furthermore, different numerical methods used different waves steepness, as presented in Section 4.4.3, making it hard to compare the results. It is not possible to conclude from this comparison that any method is significantly superior to the others for the KVLCC2 case.

When looking at the total computational time, it must be kept in mind that several encounter periods are simulated: they range between 44 for the case $\lambda = 1.4 \cdot L_{pp}$ up to 100 for the shortest waves. Some improvements for the computational time are presented in Chapter 6.

5 Conclusions

In this report, a summary of the work conducted so far within the PhD project "*Added resistance and ship motions in oblique waves*" has been presented. As discussed in Section 1.1, it is important to predict with high accuracy how a ship will react in a seaway in order to maximize its efficiency, safety and comfort. For the numerical simulations, a fully nonlinear unsteady potential flow method was used. Since the aim of the project is to evaluate added resistance and ship motions for a ship sailing in a generic sea state, the first steps consisted in limiting the number of variables and to simulate simpler conditions.

The first two papers appended focused on the prediction of roll motion using a potential flow method. Potential flow methods discard viscosity, but viscous effects can have a central role in the behaviour of roll motion. In order to account for these effects, damping coefficients were added to the equation of roll motion. In general, a good agreement between simulations and experimental results was found for roll decay, both for damping coefficients obtained from a Watanabe-Inoue method based on regression analysis and from a Parameter Identification Technique, where the coefficients are based on roll decay experiments for the hull to be computed. When it came to the prediction of roll motion in beam sea though, consistently better results were obtained using the Parameter Identification Technique for the damping coefficients, which is capable of predicting the damping coefficients with higher accuracy. For the parametric rolling, similar results were obtained with both methods for the damping coefficients, but the PIT proved again to allow a closer representation of the experiments. The results of the simulations were compared with those of other methods used to predict parametric rolling within an EU benchmark study: the code presented here proved to be in the range of the best performing ones.

For papers C and D major modifications were included in the code, such as the introduction of acceleration potential, an unstructured grid refinement and a nonlinear decomposition of the velocity potential. Simulations of ship motions and added resistance in head waves for the KVLCC2 and ship-ship interaction were carried out. The evaluation of the motions and added resistance for the KVLCC2 showed very good agreement between the simulations and experiments and other numerical methods. The simulations of the ship-ship interaction on the other hand, failed to correctly capture yaw moments and side forces. This could be due to several reasons. The cases tested were characterized by low speed and the predominant component of the longitudinal force is mainly viscous, making the potential flow method less suited than other methods. The error in the prediction of the moments can be related to the absence of circulation and separation in the potential flow, leading to an erroneous moment lever arm.

With few exceptions, the method investigated in this thesis has proven to be able to handle the tested scenarios, giving satisfactory results in terms of prediction of ship motions and added resistance in head waves. The introduction of an unstructured adaptive mesh allows for a more efficient discretization of the free surface, with finer resolution around the hull and at parts with large curvature and a coarser grid further away. This approach grants higher accuracy in critical areas, such as the vicinity of the hull, resulting in a better resolution of the flow field and increased computational efficiency. Higher computational efficiency is also enhanced by the introduction of a Banres-Hut algorithm to

the boundary element method. The next steps in order to achieve numerical simulations in oblique waves will be described in Chapter 6.

6 Future Work

In order to extend the capabilities of the method to evaluate ship motions and added resistance in oblique waves, some modifications will be made to the code. When there is an angle of attack between the ship and the incident wave direction, viscous effects start to become more important. To better handle this, a formulation which allows to account for the lift, or circulation around the hull, has to be introduced. Furthermore, introducing circulation might help in reducing the error that arose in Paper C, where this was believed to be the major cause for the failure to correctly predict the moment and side forces. As a first step, simple models will be included in the code, based on simplified theories and empirical formulations. After this, to model the lift in a more precise way, vortices or dipoles will be introduced.

With the aim of simulating free sailing in oblique waves, rudder and propeller force models will have to be introduced. The same approach used for the hull generated lift will be adopted: simpler models will initially be used, where they represent external forces acting on specific points on the body. These forces are added to the equations of motion. With this approach it is possible to easily include any type of force as long as it can be modeled in a meaningful manner. For example, forces deriving from sails and Flettner rotors can be included.

Furthermore, some improvements can be achieved in terms of computational efficiency. One way to improve the computational efficiency is to replace the current method for the acceleration potential, where one Laplace problem is solved for each degree of freedom. For 6 degrees of freedom there are more efficient ways to compute the acceleration potential, see Tanizawa, 1995.

References

Bandick P. J. & Beck R. F. (2010). The acceleration potential in fluid–body interaction problems. *Journal of Engineering Mathematics*, *70*, 147–163. https://doi.org/https://doi.org/10.1007/s10665-010-9446-0

Barnes J. & Hut P. (1986). A hierarchical O(N log N) force-calculation algorithm. *Nature*, *324*(6096), 446–449. https://doi.org/10.1038/324446a0

Bass D. & Haddara M. (1988). Nonlinear models of ship roll damping, In *Int. shipbuilding progr., 35, no. 401.*

Beck Et al. (1989). *Principles of naval architecture* (Vol. 3). The Society of Naval Architects; Marine Engineers.

Bulian G. & Francescutto A. (2013). Second generation intact stability criteria: On the validation of codes for direct stability assessment in the framework of an example application. *Polish Maritime Research.*

Contento G., Francescutto A. & Piciullo M. (1996). On the effectiveness of constant coefficients roll motion equation. *Ocean Engineering*, *23*(7), 597–618. https://doi.org/https://doi.org/10.1016/0029-8018(95)00056-9

Coslovich F., Contento G., Kjellberg M. & Janson C.-E. (2018). Computations of roll motion in waves using a fully nonlinear potential flow method, In *Nav 2018. 19th international conference on ship and maritime research.*

Coslovich F., Kjellberg M. & Janson C.-E. (2019). Prediction of parametric rolling for a container ship in regular and irregular waves using a fully nonlinear potential flow method, In *Marine 2019. viii international conference on computational methods in marine engineering.*

Coslovich F., Kjellberg M., Östberg M. & Janson C.-E. (2020). Added resistance, heave and pitch for the kvlcc2 tanker using a fully nonlinear unsteady potential flow boundary element method. *Ocean Engineering - Under Review.*

Coslovich F., Östberg M. & Broberg L. (2019). Fully nonlinear potential flow method for multiple floating bodies in confined waters, In *Icsot 2019. 6th international conference on ship and offshore technology.*

Ducrozet G., Bingham H., Engsig-Karup A. P. & Ferrant P. (2010). High-order finite difference solution for 3D nonlinear wave-structure interaction. *Journal of Hydrodynamics*, *22*(1), 225–230. https://doi.org/10.1016/S1001-6058(09)60198-0

el Moctar O., Shigunov V. & Zorn T. (2011). *Duisburg test case: Post-panamax container ship for benchmarking* (Report). University of Duisburg.

Engsig-Karup A., Bingham H.-B. & Lindberg O. (2009). An efficient flexible-order model for 3d nonlinear water waves. *Journal of Computational Physics*, *228*(6), 2100–2118. https://doi.org/https://doi.org/10.1016/j.jcp.2008.11.028

Faltinsen O., Minsaas K., Liapis N. & Skjørdal S. (1980). Prediction of resistance and propulsion of a ship in a seaway, In *Proceedings of the 13th symposium on naval hydrodynamics.*

Falzarano J., Somayajula A. & Seah R. (2015). An overview of the prediction methods for roll damping of ships. *Ocean Systems Engineering*, *5*, 55–76. https://doi.org/10.12989/ose.2015.5.2.055

Francescutto A. & Contento G. (1999). Bifurcations in ship rolling: Experimental results and parameter identification technique. *Ocean Engineering, 26.*

Gerritsma J. & Beukelman W. (1972). The excess resistance of a ship in rough seas. *International Shipbuilding Progress*, *19*, 285–293. https://doi.org/10.3233/ISP-1972-1921701

Guha A. & Falzarano J. (2015). The effect of hull emergence angle on the near field formulation of added resistance. *Ocean Engineering, 105*, 10–24. https://doi.org/https://doi.org/10.1016/j.oceaneng.2015.06.012

Hess J. & Smith A. (1967). Calculation of potential flow about arbitrary bodies. *Progress in Aerospace Sciences*, *8*, 1–138. https://doi.org/https://doi.org/10.1016/0376-0421(67)90003-6

Himeno Y. (1981). *Prediction of ship roll damping - state of the art* (Report). University of Michigan.

Hizir O., Kim M., Turan O., Day A., Incecik A. & Lee Y. (2019). Numerical studies on non-linearity of added resistance and ship motions of kvlcc2 in short and long waves. *International Journal of Naval Architecture and Ocean Engineering, 11*(1), 143–153. https://doi.org/https://doi.org/10.1016/j.ijnaoe.2018.02.015

ITTC. (2011). *Numerical estimation of roll damping* (Raccomended Procedures). 26th Specialist Committee on Stability in Waves.

Janson C.-E. (1997). *Potential flow panel methods for the calculation of free-surface flows with lift* (Ph. D. Thesis). Chalmers University of Technology.

Joncquez S., Bingham H. & Andersen P. (2008). Validation of added resistance computations by a potential flow boundary element method, In *Proceedings of the 27th symposium on naval hydrodynamics.*

Joosen W. (1966). Added resistance of ship in waves., In *Proceedings of the 6th symposium on naval hydrodynamics.*

Kang C. G. & Gong I. Y. (1990). A numerical solution method for three-dimensional nonlinear free surface problems., In *Proceedings of the 18th symposium on naval hydrodynamics.*

Kim K.-H., Seo M.-G. & Kim Y. (2012). Numerical analysis on added resistance of ships. *International Journal of Offshore and Polar Engineering, 22*, 21–29. https://doi.org/https://doi.org/10.1016/j.oceaneng.2010.12.007

Kjellberg M. (2013). *Fully nonlinear unsteady three-dimensional boundary element method for ship motions in waves* (Ph. D. Thesis). Chalmers University of Technology.

Kjellberg M., Janson C.-E. & Contento G. (2011). A nested domains technique for a fully-nonlinear unsteady three-dimensional boundary element method for free-surface flows with forward speed, In *In proceedings of the 21st international offshore and polar engineering conference.*

Kjellberg M., Janson C.-E. & Contento G. (2012). Fully nonlinear potential flow method for three-dimensional body motion, In *In proceedings of nav 2012 the 17th international conference on ships and shipping research.*

Lataire E., Vantorre M. & Delefortrie G. (2009). Captive model testing for ship-to-ship operations, In *Proceedings of marsim2009*, Panama City, Panama.

Liu S., Papanikolaou A. & Zaraphonitis G. (2011). Prediction of added resistance of ships in waves. *Ocean Engineering*, *38*, 641–650. https://doi.org/https://doi.org/10.1016/j.oceaneng.2010.12.007

Longuet-Higgins M. S. & Cokelet E. D. (1976). The deformation of steep surface waves on water - i. a numerical method of computation, In *Proceedings of the royal society a: Mathematical, physical and engineering science*, Proc. R. Soc. Lond. A.

Maruo H. (1957). The excess resistance of a ship in rough seas. *International Shipbuilding Progress*, *4*, 337–345. https://doi.org/10.3233/ISP-1957-43501

Mola A., Heltai L. & DeSimone A. (2017). Wet and dry transom stern treatment for unsteady and nonlinear potential flow model for naval hydrodynamics simulations. *Journal of Ship Research*, *61*, 1–14.

Papanikolaou A. & Spanos D. (2009). *Safedor international benchmark study on numerical simulation methods for the prediction of parametric rolling of ships in waves* (Report). NTUA-SDL.

Sadat-Hosseini H., Wu P.-C., Carrica P. M., Kim H., Toda Y. & Stern F. (2013). Cfd verification and validation of added resistance and motions of kvlcc2 with fixed and free surge in short and long head waves. *Ocean Engineering*, *59*, 240–273. https://doi.org/https://doi.org/10.1016/j.oceaneng.2012.12.016

Salvesen N. (1974). Second order steady state forces and moments on surface ships in oblique regular waves., In *Proceedings of the international symposium on dynamics of marine vehicles and structures in waves*.

Seo M.-G., Yang K.-K., Park D.-M. & Kim Y. (2014). Numerical analysis of added resistance on ships in short waves. *Ocean Engineering*, *87*, 97–110. https://doi.org/https://doi.org/10.1016/j.oceaneng.2014.05.011

Tanizawa K. (1995). A nonlinear simulation method of 3-d body motions in waves: Formulation with the acceleration potential, In *10th international workshop on water waves and floating bodies*.

Yuan Z.-M. & Yeung R. W. (2018). Unsteady interactions among multiple ships with free-surface effects, In *32nd symposium on naval hydrodynamics*.

Zou L. & Larsson L. (2013). Numerical prediction of ship-to-ship interaction in shallow water. *Ocean Engineering*, *72*, 386–402.